J. Fluid Mech. (1999), *vol.* 399, *pp.* 1–48. Printed in the United Kingdom

Self-similarity and internal structure of turbulence induced by Rayleigh–Taylor instability

By S. B. DALZIEL[1], P. F. LINDEN[1]† AND D. L. YOUNGS[2]

[1] Department of Applied Mathematics and Theoretical Physics, University of Cambridge, Silver Street, Cambridge CB3 9EW, UK

[2] AWE, Aldermaston, Reading RG7 4PR, UK

(Received 7 August 1997 and in revised form 2 November 1998)

This paper describes an experimental investigation of mixing due to Rayleigh–Taylor instability between two miscible fluids. Attention is focused on the gravitationally driven instability between a layer of salt water and a layer of fresh water with particular emphasis on the internal structure within the mixing zone. Three-dimensional numerical simulations of the same flow are used to give extra insight into the behaviour found in the experiments.

The two layers are initially separated by a rigid barrier which is removed at the start of the experiment. The removal process injects vorticity into the flow and creates a small but significant initial disturbance. A novel aspect of the numerical investigation is that the measured velocity field for the start of the experiments has been used to initialize the simulations, achieving substantially improved agreement with experiment when compared with simulations using idealized initial conditions. It is shown that the spatial structure of these initial conditions is more important than their amplitude for the subsequent growth of the mixing region between the two layers. Simple measures of the growth of the instability are shown to be inappropriate due to the spatial structure of the initial conditions which continues to influence the flow throughout its evolution. As a result the mixing zone does not follow the classical quadratic time dependence predicted from similarity considerations. Direct comparison of external measures of the growth show the necessity to capture the gross features of the initial conditions while detailed measures of the internal structure show a rapid loss of memory of the finer details of the initial conditions.

Image processing techniques are employed to provide a detailed study of the internal structure and statistics of the concentration field. These measurements demonstrate that, at scales small compared with the confining geometry, the flow rapidly adopts self-similar turbulent behaviour with the influence of the barrier-induced perturbation confined to the larger length scales. Concentration power spectra and the fractal dimension of iso-concentration contours are found to be representative of fully developed turbulence and there is close agreement between the experiments and simulations. Other statistics of the mixing zone show a reasonable level of agreement, the discrepancies mainly being due to experimental noise and the finite resolution of the simulations.

---

† Present address: Department of Applied Mechanics and Engineering Sciences, University of California, San Diego, 9500 Gilman Drive, La Jolla, CA 92093-0411, USA.

1. Introduction

Mixing between fluids can result from a variety of mechanisms such as mechanical stirring or the generation of vortical motions through shear instabilities which wrap up the iso-concentration surfaces. Density differences can lead to a stabilization or destabilization of the flow, thus either decreasing or increasing mixing, depending on the relationship between the density gradients and gravitational field. These relationships may occur as the result of initial or boundary conditions, or be produced as a side effect of other processes occurring within the flow.

Rayleigh–Taylor instability can occur whenever the density and pressure gradients are in opposite directions. Lord Rayleigh (1883) was the first to consider this problem, concentrating on an unstable stratification in a gravitational field. Subsequently, Taylor (1950) showed that any component of acceleration normal to an interface between two fluids of differing densities would produce an instability when the acceleration was towards the denser fluid. Since then Rayleigh–Taylor instability has received attention in a wide range of contexts, but many aspects of the instability are still uncertain. A review is provided by Sharp (1984), although considerable progress has been made over the last decade.

Few previous experimental studies have investigated the mixing produced by Rayleigh–Taylor instability between miscible fluids. The use of miscible fluids makes possible a detailed study of the fine-scale structure where molecular processes become important in the absence of surface tension. In addition, relatively little of the earlier work has drawn together both experimental and three-dimensional numerical models for the instability. Linden, Redondo & Youngs (1994) present possibly the most comprehensive comparison and find a broad qualitative similarity, but good quantitative agreement is lacking. This paper discusses improved experimental diagnostics and provides a higher level of interaction between experiments and numerical simulations with the numerical component designed to model the experimental flows as closely as feasible.

The physical arrangement we study is the instability between a layer of salt water of density ρ_1 initially overlying a layer of fresh water of density $\rho_2 < \rho_1$. The experimental apparatus consists of a rectangular tank of depth $H = 500\,\text{mm}$ with the two fluid layers initially separated by a barrier at half the tank depth. In order to simplify the experimental design and analysis, we focus on flows with very low Atwood numbers, $A = (\rho_1 - \rho_2)/(\rho_1 + \rho_2)$. The dimensional group $(H/Ag)^{1/2}$, where g is the acceleration due to gravity, then gives the characteristic time scale for the flows. Most of the experiments presented in this paper were conducted with $A \approx 2 \times 10^{-3}$ giving a characteristic time scale of 5 s.

Of central concern to many earlier studies of Rayleigh–Taylor instability was the growth of the mixing zone, the region where a mixture of upper- and lower-layer fluids may be found. It was believed that for many purposes a knowledge of the growth of this mixing zone was sufficient to characterize the instability. Indeed, dimensional analysis and similarity theory both predict a simple, self-similar growth for this zone in miscible fluids with negligible viscosity and diffusivity.

If the instability were to evolve from an interface which is initially flat apart from infinitesimal disturbances, then the initial growth would be linear with viscosity setting the maximum growth rate to length scales of the order of $(\nu^2/Ag)^{1/3}$ (Chandrasekhar 1961, p. 447), where ν is the kinematic viscosity. The associated time scale is $(\nu/A^2g^2)^{1/3}$. For the flows discussed in this paper these scales correspond to a length scale of the order of 1 mm and time scale of 0.1 s. This rapid e-folding of these

disturbances leads to nonlinear growth of the instability very soon after it is initiated and long before it has extended a significant fraction of the depth of the tank. During this linear growth phase the Reynolds number also increases exponentially so that viscous effects are negligible within a few e-folding time scales.

For most of the growth phase of the instability the flow is not influenced by the presence of the upper and lower boundaries of the tank. Dimensional analysis then suggests for an inviscid flow that the penetration of the lower layer into the upper half of the tank should follow

$$h_1 = \alpha_1 A g t^2, \tag{1}$$

where α_1 is a dimensionless constant. Similarly, the penetration into the lower half of the tank follows

$$h_2 = \alpha_2 A g t^2, \tag{2}$$

with an appropriate value of the constant α_2. For Boussinesq flows with $A \ll 1$ the symmetry of the problem suggests $\alpha_1 = \alpha_2$. For non-Boussinesq flows, the less-dense fluid will be more mobile than the denser fluid, resulting in $\alpha_1 < \alpha_2$.

By non-dimensionalizing the penetrations h_1 and h_2 by the depth of the tank H, we obtain

$$\delta_i \equiv h_i/H = \alpha_i \tau^2, \quad i = 1, 2, \tag{3}$$

where

$$\tau = (Ag/H)^{1/2} t \tag{4}$$

is the dimensionless time. It is observed that by $\tau = 4$ the mixing zone has reached the top and bottom of the tank and a globally stable stratification has been established. Local regions of instability remain in a combination of internal waves and decaying turbulence.

The experiments of many previous researchers (e.g. Read 1984; Youngs 1989; Kucherenko *et al.* 1991; Dimonte & Schneider 1996) have been consistent with the quadratic time dependence suggested by equation (4), at least for part of the growth phase and in high-Atwood-number immiscible fluids. Moreover, the constant α_1 has been found to be independent of Atwood number over a wide range of Atwood numbers, with a typical value of $\alpha_1 \approx 0.06$. In contrast α_2 is found to increase slowly with the Atwood number. With miscible fluids at low Atwood number the picture is less clear. Linden *et al.* (1994) and Dalziel (1993) both present evidence that while the growth rate has a τ^2 component, the true picture is somewhat more complex. The departure from the expected quadratic dependence has been attributed to the initial conditions, but the relationships and mechanisms have not been extracted.

Detailed comparisons with numerical simulations of the internal structure for mixing of miscible fluids are not available. Redondo & Linden (1993) discuss some aspects, as do Linden *et al.* (1994), but these comparisons have experimental limitations. Through the combination of an improved experimental setup and the use of image processing techniques, the present paper attempts to rectify this situation.

In § 2 the experiments are described and the key features of the initial conditions they produce are analysed. The details of these initial conditions are then incorporated in the numerical simulations which are introduced in § 3. An overall qualitative comparison of the experimental and numerical results is presented in § 4, before considering the growth of the mixing zone in § 5. Details of the density structure within the mixing zone are described in § 6, while § 7 discusses the statistical properties of the mixing produced. Finally our conclusions are given in § 8.

2. Experiments

The experimental apparatus was chosen to provide a simple way of investigating the mixing of miscible fluids. Optical diagnostics have been used to measure the fine-scale structure and this necessitates the use of two fluids with the same refractive index. Other requirements are that the boundary conditions should be well-defined and the initial conditions should contain as little disturbance as possible. In addition, the flow should evolve over a time scale sufficiently short to render viscous effects unimportant, but sufficiently long to enable accurate quantitative diagnostics using image processing techniques. These requirements have led to the choice of an experiment using two aqueous solutions. Refractive-index matching then implies that a low Atwood number ($A \ll 1$) must be used.

Well-defined initial conditions may be achieved by starting with a stable stratification and then accelerating the test chamber downwards to obtain an unstable acceleration. This approach has been used by Read (1984), Kucherenko *et al.* (1991) and Dimonte & Schneider (1996). However, few of the experiments have used miscible liquids and, with this technique, it is difficult to use the low Atwood number needed for refractive index matching, because of the long acceleration distance then required for significant mixing to occur.

A number of other researchers (e.g. Andrews & Spalding 1990; Voropayev, Afanasyev & van Heijst 1993) have tried inverting a stable stratification. Unfortunately, unless the fluid is very viscous, Kelvin's circulation theorem shows that it is not possible to achieve the desired unstable initial stratification. In a circular cylinder rotated about its (horizontal) axis, the rotation will leave the stratification in its initial configuration (except in thin boundary layers near the walls). At the other limit, with a tall narrow container, it is possible to achieve an unstable stratification in this way, but the initial orientation of the interface is at an angle of $\tan^{-1} 2\pi$ to the horizontal (Simpson & Linden 1989), representing a substantial departure from ideal initial conditions.

These considerations have led to the choice of a static tank with the denser layer of fluid initially above the layer of less-dense fluid, these layers being separated by a barrier. The use of a static tank makes the diagnostics easier and apparatus simpler. However, there is an inevitable disadvantage: removal of the barrier creates a significant initial disturbance. The design of the barrier (see § 2.1) has been chosen to minimize this disturbance and a detailed analysis of the effect of barrier removal on the development of the instability is presented. In many industrial and environmental situations statically unstable turbulent mixing evolves from non-ideal initial conditions and we suggest that the study of the effect of initial conditions found in the present apparatus contains useful lessons for a broader class of problems.

2.1. *Experimental method*

The experiments were performed in the tank shown in figure 1. This tank is $L = 400\,\text{mm}$ long, $W = 200\,\text{mm}$ wide and has a working section $H = 500\,\text{mm}$ deep. One endwall of the tank is slotted and the sidewalls are grooved in order that a barrier may be inserted at half the tank depth, dividing it into two equal volumes. A floating lid is positioned at the top of the upper layer to provide a rigid boundary which allows the water level to adjust as the barrier is withdrawn.

Conventional barriers, such as that used by Linden *et al.* (1994), comprising a single rigid sheet to separate the two layers have the disadvantage of viscous boundary layers forming on their upper and lower surfaces as the barrier is withdrawn. The wake left behind the barrier due to these shear layers introduces a long-wave disturbance to

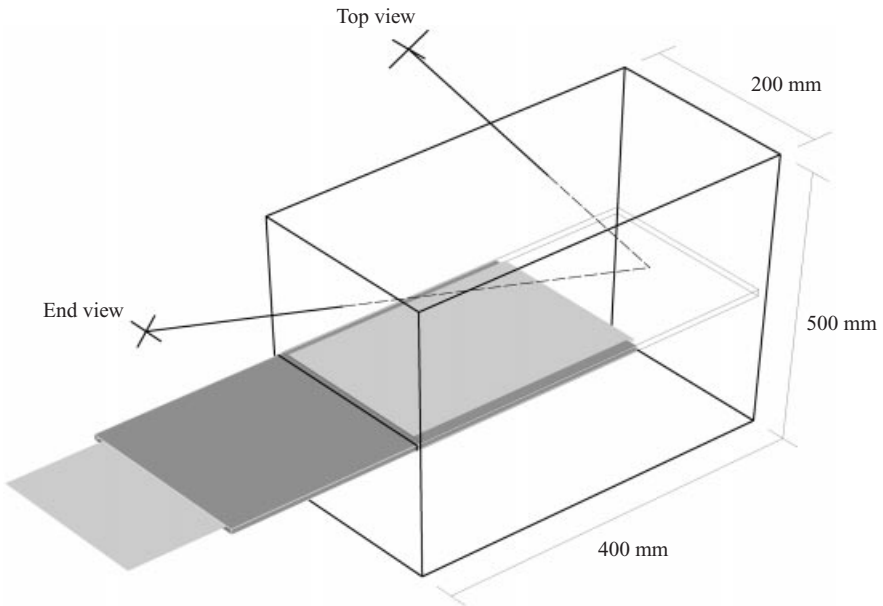

FIGURE 1. Sketch of experimental apparatus. The hollow stainless steel barrier is shown as dark grey and the nylon fabric as light grey. The orientation of the perspective views presented in § 4.2 are also indicated.

the initial conditions. The viscous boundary layers are also stripped off the barrier by the endwall of the tank to form a pair of strong vortices propagating away from the barrier (Dalziel 1994*b*).

The design of the barrier used for the experiments reported here was conceived by Lane-Serff (1989) in an attempt to eliminate shear layers forming on the two surfaces of the barrier, and has been used previously by Dalziel (1993, 1994*a*, *b*) for Rayleigh–Taylor instability. The barrier consists of a flat, rigid tube made of stainless steel (shaded dark grey in figure 1) through which two pieces of nylon fabric (shaded light grey) are passed. One piece of fabric is stretched along the upper surface of the stainless steel to be attached to the endwall of the tank immediately above the slot in the endwall. The second piece of fabric is similarly stretched over the lower side and also attached to the endwall of the tank. When the tube is withdrawn, the nylon fabric immediately above and below remains motionless, except that as the end of the tube passes a given point, the nylon fabric at that point is pulled in and removed along the centre of the tube. Thus, except for the passage of the end of the barrier, the fluid in the tank sees the barrier as a motionless boundary. Unfortunately, the construction of the barrier meant there was a 10 mm wide strip down each side of the barrier which was not protected by the nylon fabric. As we shall see later in § 4.1, this feature affects the flow at the later stages in its development. Details of the initial conditions resulting from this barrier are presented § 2.3.

The barrier was withdrawn at the start of each experiment by pulling manually on the nylon fabric passing through the length of the barrier while simultaneously pushing inward on the outer end of the barrier. The withdrawal rate was found to be repeatable to within 10%. For the majority of experiments presented here a withdrawal rate of $U_{Barrier} \approx 200\,\mathrm{mm\,s^{-1}}$ was selected, giving a withdrawal time of $t_0 \approx 2\,\mathrm{s}\,(\tau_0 \approx 0.4)$.

Prior to the start of the experiment the volume below the barrier is filled with a solution of water and propan2ol, while the volume above is filled with a salt-water solution. The alcohol was used to match the refractive index between the two bodies of fluid. An adequate level of matching was achieved with 3 ml of propan2ol in the lower layer for every 1 g salt in the upper layer. The initial density of the two layers was measured using a Paar densitometer to determine the Atwood number. This Atwood number was repeatable to within 5% between one experiment and the next. The LIF (light-induced fluorescence) experiments presented here were all performed with an Atwood number of $A = 2 \times 10^{-3}$ (giving a time scale of 5 s) whereas the perspective experiments were run with $A = 7 \times 10^{-4}$ (and a correspondingly longer time scale).

The solutions were preconditioned by exposing them to a 300 m bar vacuum overnight in order to allow them to reach thermal equilibrium with the laboratory and remove most of the dissolved air to prevent a plume of bubbles forming at the trailing edge of the barrier during the removal process.

2.2. *Measurement techniques*

Three techniques were used to provide diagnostics for the experiments: computer-enhanced light-induced fluorescence, particle tracking and perspective views.

2.2.1. *Light-induced fluorescence*

Most of the results reported in this paper were obtained using light-induced fluorescence (LIF). The dense layer was doped with a small quantity of sodium fluorescein (a green fluorescent dye) and the flow illuminated from below by a thin light sheet oriented as a vertical plane centred halfway across the width of the tank. A high-resolution, frame integration monochrome CCD video camera was used in conjunction with a 1/100 s mechanical shutter to give full frame resolution video images of the flow. The video signal was recorded on Super VHS video tape for later analysis.

Normally a laser is used as the light source for LIF flow measurements. However, here the light sheet was produced by a 300 W xenon arc lamp, collimated by an integral parabolic reflector into a slowly diverging beam. The degree of collimation provided by the light source allowed light sheets as thin as 0.5 mm to be produced throughout the depth of the tank. For the experiments reported here a light sheet 2 mm thick was used to increase the intensity of the LIF images and thus allow the video camera to be operated at a lower gain.

The illumination provided by the light sheet was not, however, uniform. The intensity along the bottom of the tank varied by a factor of four. This variation was exaggerated further up the tank with the along-tank divergence of the sheet (practical considerations prevented the arc lamp being positioned any further back to allow only the central spot to be used). In addition, the concentration of fluorescent dye required to provide an image of sufficient intensity for the video camera was such that there was a significant attenuation of the light sheet as it passed through the dye. Image processing techniques (Dalziel 1994*b*) were used to correct for the attenuation and divergence of the light rays prior to extracting quantitative information.

2.2.2. *Particle tracking*

The velocity measurements presented in § 2.3 were obtained using the particle tracking technique described in Dalziel (1992, 1993). For these experiments the flow was seeded with neutrally buoyant 250 μm diameter Pliolite VTAC particles and

illuminated with a light sheet in the same manner as described for the LIF experiments. The seeding density was such that around 3000 particles were visible in the light sheet at any one time, and these particles were tracked to obtain their Lagrangian paths while they remained within the light sheet. The randomly distributed velocity data obtained in this manner were then mapped onto a regular Eulerian grid using a weighted least-squares technique.

2.2.3. *Perspective views*

To produce the perspective views presented in § 4.2, the lower layer was dyed with a concentrated mixture of red and blue food colouring, to render it nearly opaque with light unable to penetrate further than a depth of around 1 mm. Sodium fluorescein dye was also added so that the surface of the dyed region fluoresced under the illumination of the xenon arc lamp. The net result of this cocktail of dyes was to give the lower layer a solid appearance, even when diluted significantly by upper layer fluid.

2.3. *Initial conditions*

As described in § 2.1, the purpose of the nylon fabric wrapped around the barrier was to present the fluid above and below the barrier with a stationary surface as the barrier was removed. Unfortunately, the barrier does introduce perturbations to the flow caused by the motion of the nylon around its trailing edge, and the removal of the finite volume associated with it. Of these two the volume-driven component is the more important, even though the barrier represents only 0.5% of the total volume of the tank.

2.3.1. *Mechanism*

The effect of removing the finite volume associated with the barrier may be understood most readily by considering an unstratified flow. As the barrier is removed, the upper layer moves downward to replace the volume of the barrier no longer in the tank. The floating lid forces this motion to be essentially uniform along the length of the tank. While there is a potential energy change associated with the change in free-surface height, it is exactly balanced by the work done on the barrier by the hydrostatic component of the pressure field acting on the end of the barrier, and may thus be ignored.

If the barrier is withdrawn at a constant velocity, then the upper layer adjusts downwards at a constant velocity. However, at the level of the barrier, the area over which this adjustment is made depends on how far the barrier has been withdrawn. At the initial instant this area is vanishingly small, inducing extremely large velocities towards the trailing edge of the barrier. With the barrier further out, the horizontal area over which the adjustment takes place is increased, reducing the magnitude of the velocities.

The stationary nature of the nylon fabric in contact with the water and the short time scale for barrier withdrawal suggest that the leading-order flow will respond inviscidly. By replacing the moving barrier with a fixed barrier plus mass sink we may make a first attempt at modelling this process by ignoring density differences and using two-dimensional potential flow theory. Figure 2 shows the velocity field resulting from this model near the beginning and end of the removal process. The key features to note here are the reduction in the magnitude of the vertical velocities and increased penetration of the flow into the lower layer as the barrier is removed further.

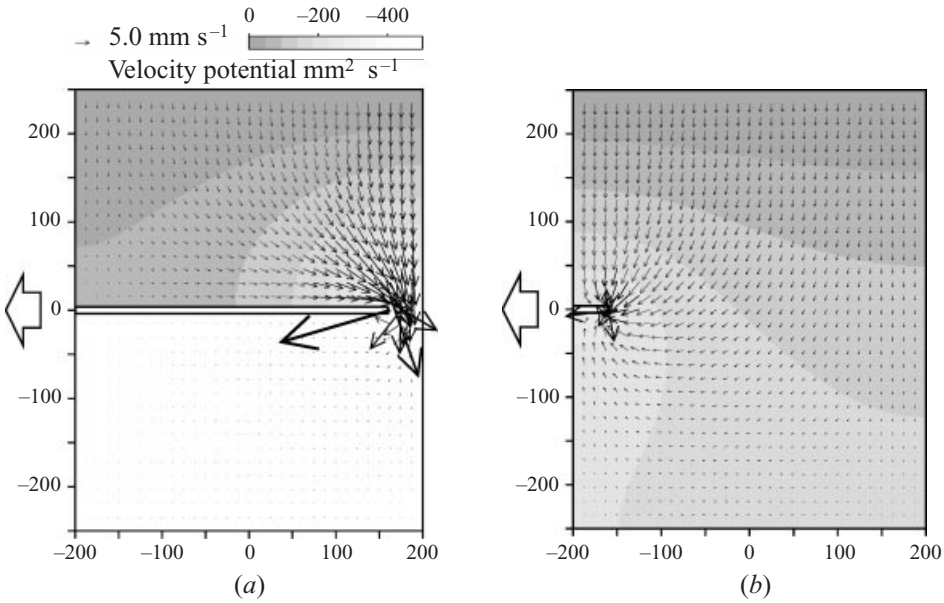

FIGURE 2. Potential flow model for the removal of the barrier. Velocity vectors are shown superimposed on a greyscale representation of the velocity potential. The barrier is shown when (*a*) 10% and (*b*) 90% withdrawn.

The potential flow model predicts its own failure. There is a clear jump in the horizontal component of the velocity across the barrier near the trailing edge, and this velocity is oriented towards the trailing edge (which is itself moving in the opposite direction). As a result the fluid is forced to turn a sharp corner and decelerate (relative to the trailing edge) at the trailing edge which, for real fluids, would lead to separation and vorticity. Another shortcoming of the potential flow model is the instantaneous nature of the velocity field. If the withdrawal of the barrier is stopped, the velocity field instantaneously returns to zero. Resolution of these problems is found in the Kutta condition. While Kelvin's circulation theorem prevents vorticity being generated within a closed fluid contour, the flow associated with the barrier provides the ability to close previously open contours and thus allow vorticity to be injected into the flow by the trailing edge of the barrier. If we can ignore precise details of what is happening at the trailing edge we may model this effect as the injection of a vortex sheet behind the barrier, the changing strength of the vortex sheet being derived from the velocity jump across the barrier as it is removed.

2.3.2. *Measurements*

Experimental measurements have been made of the flow produced by the barrier to confirm the mechanism outlined in the previous subsection and provide details of the additional structure provided by the advection of the vortex sheet and the motion of the nylon fabric around the trailing edge. These measurements were obtained by tracking neutrally buoyant particles in an unstratified flow.

Figure 3 shows the velocity field and the streamfunction obtained from one such experiment. For a streamfunction to exist, the in-plane flow should be divergence free. Calculation of $\partial u/\partial x + \partial w/\partial z$ shows that due to small three-dimensional effects this is only approximately true. We therefore construct an approximate streamfunction by integrating the velocity field iteratively under the assertion that ψ at a particular point

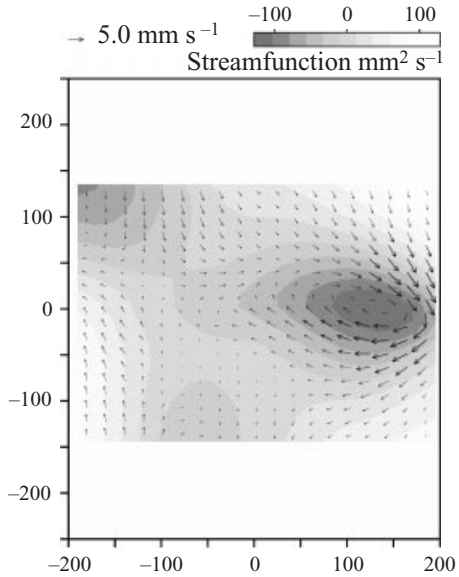

FIGURE 3. Elevation showing the velocity field induced by the removal of the barrier in a typical homogeneous experiment. The full length of the tank is shown but only the central 50% of the height. The velocity vectors are superimposed on the approximate streamfunction for this nearly two-dimensional flow.

is the mean of values obtained by integration of u and w from the four surrounding points. This procedure minimizes the energy discrepancy between the measured velocity field and calculated streamfunction. The underlying two-dimensionality of the flow has been confirmed by homogeneous experiments using the LIF technique with two light sheets spaced across the tank. In these experiments scales with a wavelength as small as 10% of the length of the tank are observed to be essentially two-dimensional, although finer scales exhibit a three-dimensional character.

An ensemble of homogeneous experiments similar to that shown in figure 3 was performed. While there was considerable scatter in the precise velocities, the overall structure of the flow, at least near the barrier $z = 0$, was consistent. The scatter may be attributed to three aspects of the experiments: variations in the barrier withdrawal rate, residual motion in the tank prior to withdrawing the barrier (it was not possible to allow the fluid to come completely to rest due to variations in the particle densities leading to particles settling or rising out) and random fluctuations in the trailing-edge condition.

2.3.3. *Combined model*

The symbols in figure 4 plot the streamfunction at $z = 0$ for ten experiments similar to that shown in figure 3. Also shown in this figure are least-squares fits to these data using the first ten Fourier (sine) modes. While these fits do not capture all the structure of the streamfunction at $z = 0$, they do capture the essential overturning and intermediate wavelengths.

To simplify the use of these experimental initial conditions in numerical simulations, we shall impose the linearity assumption that the vortex sheet is not advected while the barrier is being withdrawn. We thus confine all the vorticity to $z = 0$ and can extend the flow from the $z = 0$ streamfunction to the remainder of the tank using

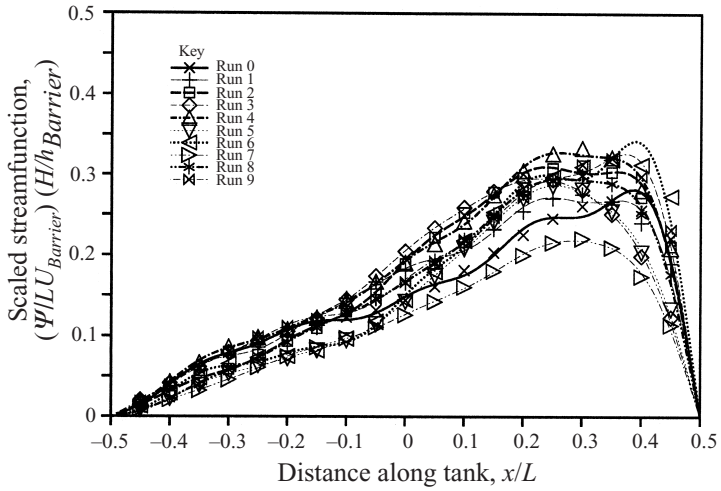

FIGURE 4. Streamfunction at $z = 0$ for 10 homogeneous experiments (marks). Least-squares fits using the first ten Fourier modes are also indicated (lines).

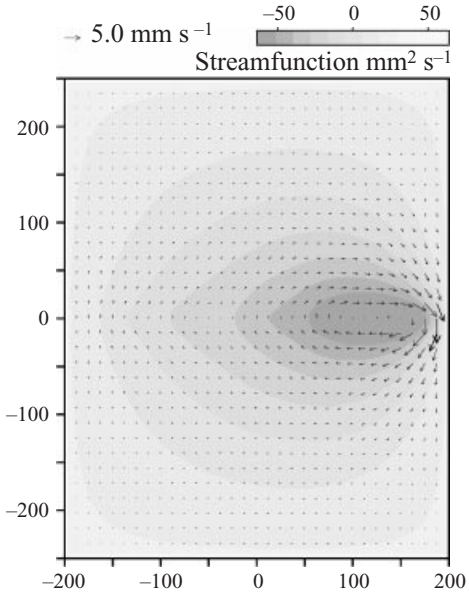

FIGURE 5. Flow induced by the vortex sheet model initialized from a homogeneous experiment.

two-dimensional irrotational flow. This results in the initial conditions being modelled as

$$\psi(x,z) = \psi_0 U_{Barrier} L \frac{h_{Barrier}}{H} \sum_{n=1}^{N} a_n \sin\frac{n\pi x}{L}\ \frac{\sinh(n\pi H/2L)(1-2|z|/H)}{\sinh(n\pi H/2L)}, \qquad (5)$$

where $N = 10$, a_n are the fitted Fourier coefficients and ψ_0 is an order-one dimensionless constant which, in practice, is a function of the barrier Reynolds number. Here we assume $\psi_0 = 1$. The flow field obtained from this irrotational extension to the experimental initial conditions is shown in figure 5 for the experiment presented

in figure 3. Comparison between these two figures shows differences in the details, due primarily by the advection of the vortex sheet, but good similarity in the main features. The agreement between these plots is comparable with that between two nominally identical experiments, showing the error in this approach to be of the order of the random variation between experiments. As we shall see in § 4, the choice of $N = 10$ for (5) recovers the relatively strong wavenumber-5 component observed in the experiments and avoids the introduction of Gibbs phenomenon or other features resulting from under-resolving the initial conditions.

3. Numerical simulations

The numerical aspects of this work have been performed with the TURMOIL3D computer program (Youngs 1991), as was used by Linden *et al.* (1994) in their comparison between experiments and simulations. Details of the initial conditions and the precise manner in which the code was set up for the work presented here differ from that used in the earlier study and so some further description is given here.

3.1. *TURMOIL3D*

The TURMOIL3D code uses an explicit method to solve the compressible Euler equations plus an advection equation for the mass fraction of fluid 1. The experiments, in which the flow is incompressible, are simulated by choosing the initial sound speed high enough to eliminate any dependence on Mach number. The numerical density ratio $\rho_1/\rho_2 = 1.2$ has been chosen to be large enough to ensure that the small density fluctuations due to compressibility of the simulated flow have little effect, while at the same time ensuring that the density difference is sufficiently small for the Boussinesq approximation to remain valid and the results to be independent of the actual values of the density except for a scaling of the buoyancy terms and related time scales.

The numerical Schmidt number, $Sc = \kappa/\nu$, where κ is the mass diffusivity and ν is the kinematic viscosity, is of order unity whereas in the experiments $Sc \sim 10^3$. However, the Reynolds number in the experiments is thought to be high enough for the properties of the fine-scale mixing to be insensitive to the Schmidt number. Hence the comparison between simulation and experiment is considered to be valid.

Advection of all fluid variables is calculated by using the monotonic method of van Leer (1977). As argued by Linden *et al.* (1994), this gives a numerical scheme with many properties essential for the present application. For example, the fluid density, which is initially discontinuous, stays in the interval $[\rho_1, \rho_2]$ thereby avoiding spurious buoyancy-generated turbulence. The monotonicity constraints in the advection method imply that there is nonlinear dissipation inherent in the numerical scheme which acts at a length scale of order the mesh size. An additional sub-grid model is therefore not needed to provide the required dissipation of density and velocity fluctuations by the unresolved scales. It is assumed that fluid is molecularly mixed at the grid scale to produce a density depending linearly on the volume fraction or concentration C of fluid 1.

The computational domain is $0 < x < L$, $0 < y < \frac{1}{2}L$, $-\frac{1}{2}H < z < \frac{1}{2}H$ and a uniform, isotropic mesh of size Δx was used with $160 \times 80 \times 200$ zones to mimic the aspect ratios found in the experiments. Reflective boundary conditions (i.e. no flow normal to the boundaries) are used on all sides of the box and the barrier is assumed to be removed in the negative x-direction (i.e. towards the left). Tests of the code using different resolutions (in both two- and three-dimensional runs – see below)

demonstrate that the results presented in this paper are not an artefact of the mesh size.

3.2. *Idealized initial conditions*

Simulations starting from two different types of initial conditions were run. The first type utilized idealized initial conditions consisting of an initial velocity field $\boldsymbol{u} = \mathbf{0}$ and a random perturbation to the interface height described by $z = \eta(x, y)$. The latter consists of a sum of Fourier modes with wavelengths in the range $4\Delta x$ to $8\Delta x$ and randomly chosen amplitudes. The standard deviation of the amplitude of these perturbations is $\sigma = 0.08\Delta x = 3.2 \times 10^{-4} H$, which has been found to be just sufficient to initiate the classical $\alpha A g t^2$ growth (see equation (1)) of the mixing zone. We shall refer to these as *idealized* simulations.

The amplitude of the initial perturbation to the interface height is sufficiently small that it is represented in the simulations simply as a random concentration fluctuation in the meshes adjacent to the $z = 0$ plane. The overall mixing rate is virtually independent of which set of random amplitudes is chosen. Further, while the early stages of evolution of the mixing zone depend on the standard deviation and wavenumber spread of the random perturbations, the subsequent loss of memory of the initial conditions and establishment of quadratic temporal growth have been found to be robust features (Youngs 1991).

3.3. *Real initial conditions*

The second set of initial conditions is based on a combination of the conditions derived from the homogeneous experiments reported in § 2.3 and the idealized initial conditions of § 3.2. In this way it is intended to capture the key features of the experimental initial conditions without the need to resort to full three-dimensional measurements of them. We shall refer to these as *barrier* simulations.

The incompressible, irrotational extension of the experimental $z = 0$ streamfunction (5) was used to initialise the x- and z-components of the velocity field and the y-component was set identically to zero. This modelled the two-dimensional component of the experimental initial conditions at low wavenumbers. To trip the three-dimensionality of the Rayleigh–Taylor instability and provide the high-wavenumber component to the experimental conditions lost through the fitting process, the same random perturbation to the interface $z = \eta(x, y)$ as used for the idealized initial conditions was also applied.

No attempt was made to match the power levels between the experimental velocity field and the random interface perturbation. Indeed, such a matching would be difficult unless both components of the perturbation were applied to the same aspect of the initial conditions and there were three-dimensional experimental measurements available. In the absence of such matching, care must be taken to ensure the memory of the higher-wavenumber aspects of the experimentally derived initial conditions is lost during the evolution of the simulations. Indeed, it was found that more of the initial two-dimensional structure was retained by the simulations than was observed at later times in the experiments, especially when comparing ensemble averages for the experiments with cross-tank averages for the simulations. In order to reduce the contamination of our results by this memory, three different sets of initial conditions, each corresponding to a different homogeneous experiment, were used to initialize different runs of TURMOIL3D. The statistical results presented are the ensemble average of these runs.

4. Qualitative results

In this section we describe the evolution of the flow from a qualitative (pictorial) viewpoint to compare the gross similarities and differences between the experiments and the two types of simulation.

4.1. *Plane sections*

Figure 6 presents a sequence of LIF images of the experiments above the corresponding planar sections for the two types of simulation. The experimental images have been corrected for the attenuation and divergence of the illuminating light sheet and show only the lower half of the tank in order to improve the spatial resolution. The lower half of the tank was selected so that the more interesting flow structures resulting from the initial conditions could be observed. These images suffer from noise at either end of the tank (especially the left-hand end) due to the low intensity of the illuminating sheet in these locations. The simulation output is for a single $y = \text{const.}$ plane in the interior of the flow and is visualized with the same relationship between concentration (volume fraction) and greyscale as obtained from the fluorescent dye in the experiments.

The barrier-induced overturning motion is clearly visible in the LIF images. The dominant feature is a plume of dense fluid descending down the right-hand endwall of the tank. The growth rate of this plume is approximately a factor of two faster than the flow in the interior of the tank. The formation of this plume is visible from the initial instant at which the barrier withdrawal starts, and by $\tau = 1$ (figure 6*a*) it is well established with a horizontal length scale small compared with the vertical scale. Perturbations to the interface at other wavelengths with a smaller amplitude are also visible. Principal among these are modes with wavenumbers 3 to 6. Both homogeneous experiments and unstable Rayleigh–Taylor runs with twin light sheets suggest that these length scales are the result of predominantly two-dimensional disturbances produced by the withdrawal of the barrier. Superimposed on these large scales are smaller-scale three-dimensional modes. Interaction of these modes both with other three-dimensional modes and the larger-scale two-dimensional modes leads to the rapid breakdown of the disturbances introduced by the barrier except at the largest scales. By $\tau = 2$ (figure 6*b*) only the components with wavenumbers 1 to 3 survive with an appreciable amplitude. The breakdown of these scales would require the three-dimensional motion to grow to a comparable level for intense nonlinear interactions. However, the sidewalls of the tank block the growth of three-dimensional motions on these scales, which, combined with the initially large difference in both scale and energy between these modes and the dominant overturning motion, imply that the two-dimensional barrier-induced motion is likely to survive.

Once the plume down the right-hand endwall reaches the bottom of the tank it forms a gravity current propagating towards the left along the tank floor. This gravity current is highly turbulent and entrains lower-layer fluid, as can be seen from the wealth of small-scale structure within it (figure 6*c*). The fluid in the lower quarter of the tank towards the left-hand end remains essentially unmixed until the gravity current is approximately 50% of the distance across the floor. At this stage in the experiments a volume of (mixed) upper-layer fluid enters the light sheet. This fluid originates from motion induced in the strip along each side of the barrier not protected by the nylon fabric. The shear between the barrier and the fluid in this strip causes a much higher initial growth rate than in the central body of the experiment. This un-modelled three-dimensional component to the initial conditions does not influence the development of the instability on the centreline of the tank until the

(*a*) (*b*)

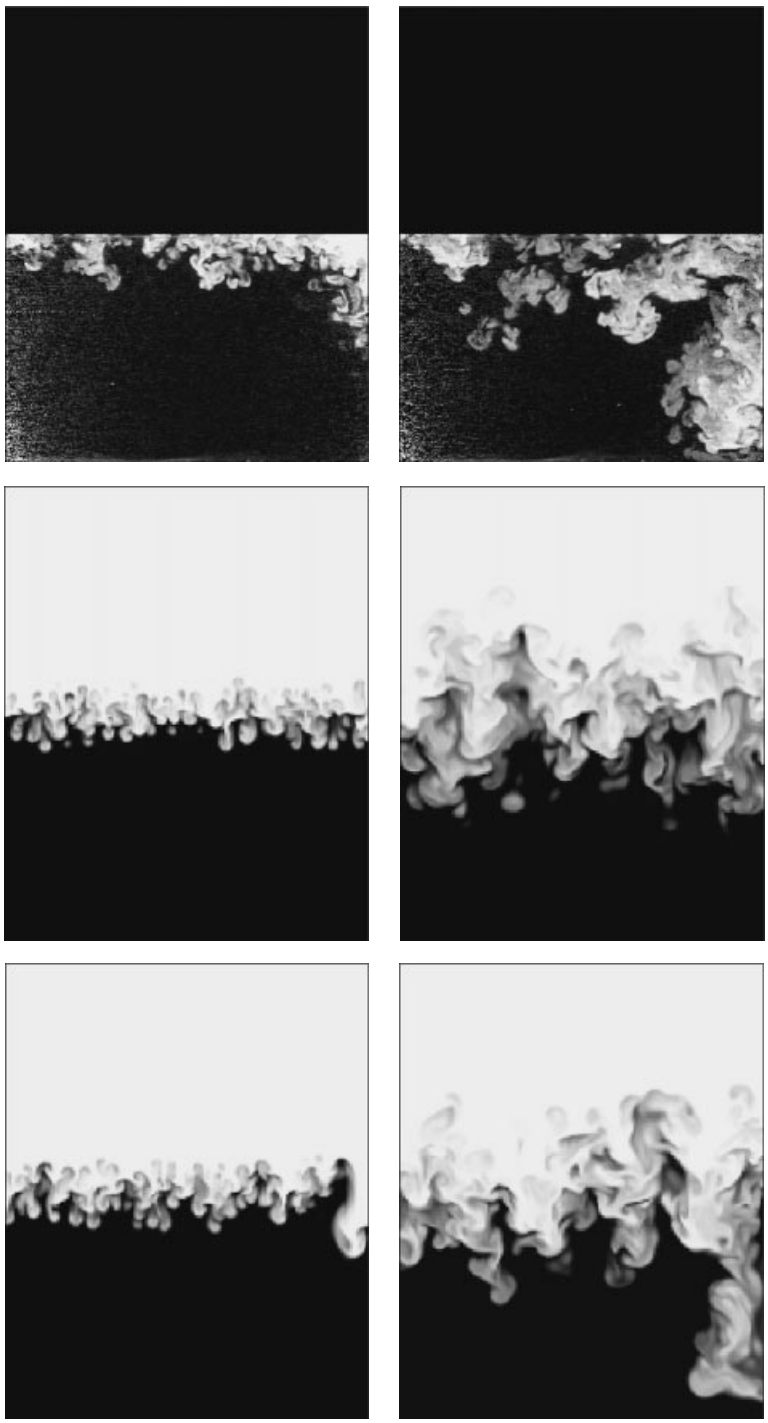

FIGURE 6(*a*, *b*). For caption see facing page.

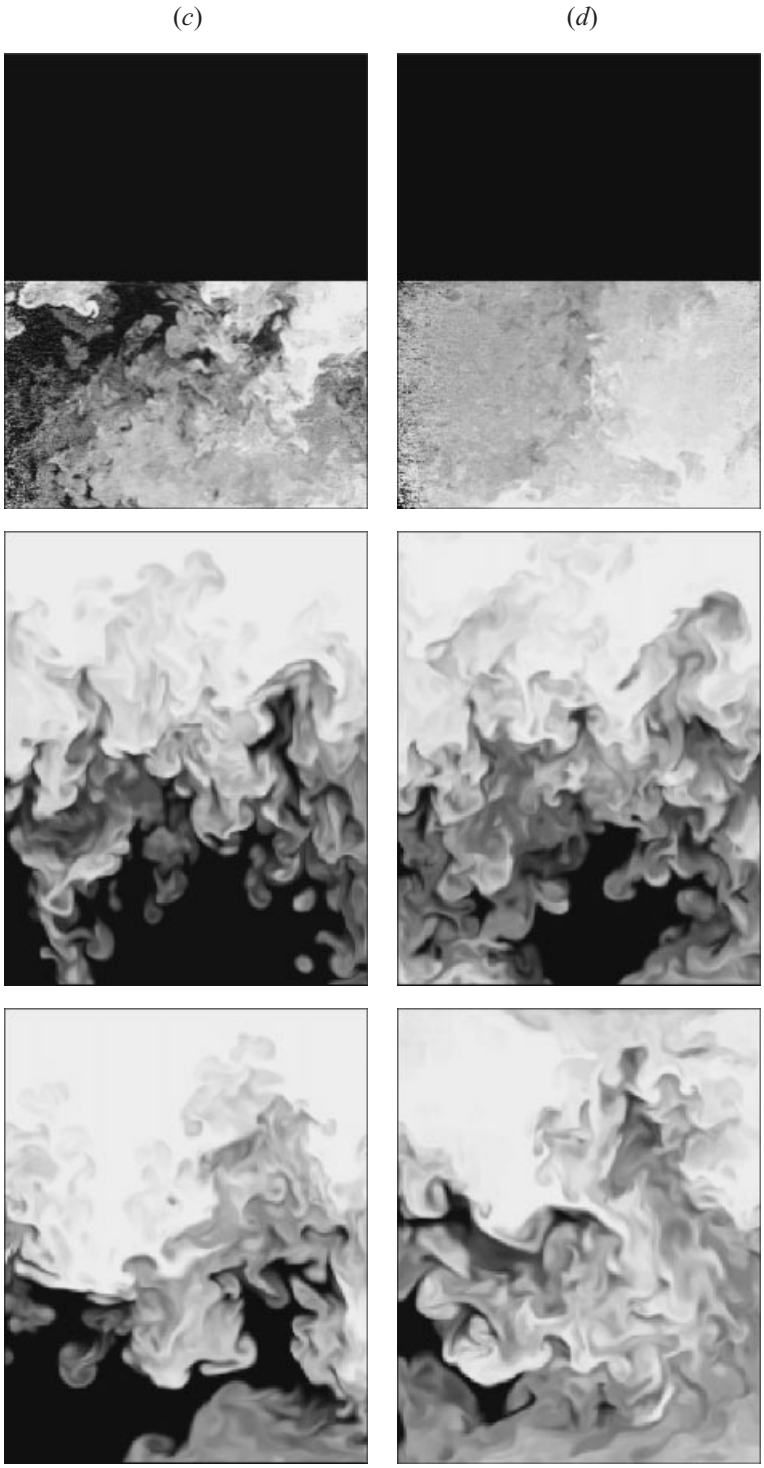

FIGURE 6. Comparison between a typical experiment (top) and simulations using idealized initial conditions (middle) and initial conditions measured from experiments (bottom). The flows are shown for (*a*) $\tau = 1$ ($t = 5$ s), (*b*) $\tau = 2$ ($t = 10$ s), (*c*) $\tau = 3$ ($t = 15$ s), and (*d*) $\tau = 4$ ($t = 20$ s). Note that only the flow in the lower half of the tank is shown for the experiment.

lateral length scale is comparable with the dimensions of the tank when the main growth phase of the instability is over.

Once the gravity current has crossed the floor of the tank (figure 6*d*) the initially two-layer unstable stratification has reached a globally stable state and the mean density of the fluid decreases with increasing height. Regions of locally unstable stratification remain embedded within this stable density gradient, providing the potential energy for additional small-scale mixing.

The central set of images in figure 6 are for simulations with idealized initial conditions. In contrast with the experiments, the width of the mixing region grows uniformly along the length of the tank. While a dominant scale can be detected at each time shown in the figure, this scale is less distinct and at higher wavenumbers than that found in the experiments. The penetration and length scales grow more slowly than found in the experiments, with the flow first touching the bottom of the tank at $\tau \approx 2.7$ compared with the $\tau \approx 2.0-2.2$ for the experimental flow. For the particular $y = \text{const.}$ plane shown here, the mixing region first reaches the bottom at the left-hand end (figure 6*c*) shortly before doing so at the right-hand end. Unmixed lower-layer fluid remains at the bottom of the tank even after $\tau = 4$. The gross character of the flow is independent of the location of the plane being viewed, although, as expected, there are differences in the detailed structure.

The barrier simulations are shown in the bottom panel of figure 6. The visual similarity with the experimental LIF images is striking. While there are differences at the small and intermediate scales, the gross overturning, the time scale to reach the bottom of the tank, and the dilution of the two fluids agree remarkably well. Although the experimental images presented here show only the lower half of the tank, comparison with additional runs showing either the upper half or the entire tank show a similar level of qualitative agreement in the upper half. The variations between this simulation and the experiment shown in figure 6 is comparable with the variations between nominally identical experiments. Furthermore, using initial conditions from a different homogeneous barrier experiment chosen at random from the set shown in figure 4 does not alter the level of similarity.

The simulations have been used to demonstrate that the time required for the mixing zone to extend to the bottom of the tank is only a weak function of the strength of the perturbation, which is, in turn, related to the withdrawal speed of the barrier $U_{Barrier}$ through (5). This equation suggests a time scale of $H^2/U_{Barrier}h_{Barrier} \sim 500\,\text{s}$ for the 'mixing zone' to reach the bottom of the tank in the absence of a density-driven flow, considerably longer than the $(H/Ag)^{1/2} \sim 5\,\text{s}$ time scale for the Rayleigh–Taylor flow. As a result, varying the amplitude of the initial perturbation (i.e. $U_{Barrier}$) by a factor of two in either direction makes only a small (less than 7%) difference to the length of the growth phase in the simulations.

As noted in § 3.1, the resolution of the numerical simulations presented here is believed to be adequate and does not influence the conclusions drawn in the comparison between the experiments and simulations. Indeed, for external measures of the flow such as typified by h_2, the barrier simulations achieve close agreement even for low-resolution two-dimensional simulations. This point is illustrated by figure 7 which presents the concentration field at $\tau = 2$ for two-dimensional simulations at resolutions of 80×100 (figure 7*a*) and 160×200 (figure 7*b*) as well as the full three-dimensional barrier simulations at $160 \times 80 \times 200$ (figure 7*c*). The overall growth of the mixing zone is virtually indistinguishable between these three simulations, the differences occurring at the finer scales. This agreement is the result of the external features of the flow being dominated by the two-dimensional component of the initial

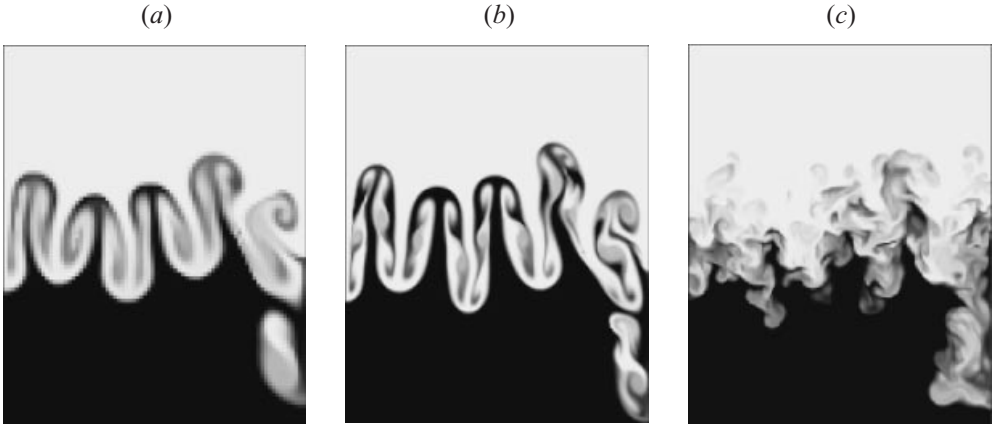

FIGURE 7. Comparison between barrier simulations performed at different resolutions. (*a*) Two-dimensional, 80×100 zones, (*b*) two-dimensional, 160×200 zones and (*c*) three-dimensional, $160 \times 80 \times 200$ zones.

conditions, and this component being well resolved even at relatively low resolutions. However, the internal structure of the flow, which results from nonlinear three-dimensional interactions, requires a full three-dimensional simulation to capture it. In two dimensions, increasing the resolution increases the generation of the finest scales resulting from shear instabilities at the boundaries between $C = 0$ and $C = 1$ fluid, but this does not mimic the three-dimensional turbulence present in the experimental flow or three-dimensional simulations.

The experiments contain finer scales than can be resolved by the simulations. Linden *et al.* (1994) have shown that the evolution of the instability in idealized simulations is sensitive to the mesh resolution due to processes at the finest scales. Tests using realistic initial conditions and different mesh resolutions have shown that the dominant behaviour of the two-dimensional component in the barrier simulations greatly reduces this resolution dependence, and that the resolution of the current simulations is more than adequate for most aspects of the flow.

Figure 8 repeats the sequence shown in figure 6 but here showing the mean concentration from an ensemble of sixteen LIF experiments (top panel), the cross-tank mean for the idealized simulation with a single set of random modes (middle panel), and the cross-tank mean for an ensemble of three barrier simulations. The members of the ensemble for the barrier simulations all used the same high-wavenumber spectrum for the initial interface displacement but different two-dimensional barrier-induced components (as indicated in figure 4). The ensemble of barrier simulations was introduced to model the variety of initial conditions found in the experimental ensemble more accurately. In addition, the use of an ensemble reduces the need to match the power levels in the two- and three-dimensional components of the initial perturbations.

The gross, large-scale features seen in the individual experiments and slices of figure 6 are maintained in the averaged images. For the experiments (top) and barrier simulations (bottom) the large-scale overturning develops as before. The wavenumber-2 component of the flow remains visible, but the higher wavenumber components are largely smeared out by random variations between the initial conditions. The mixing region for these two scenarios touches the bottom of the tank first at the right-hand end to form a gravity current propagating towards the left along the bottom of the

(*a*) (*b*)

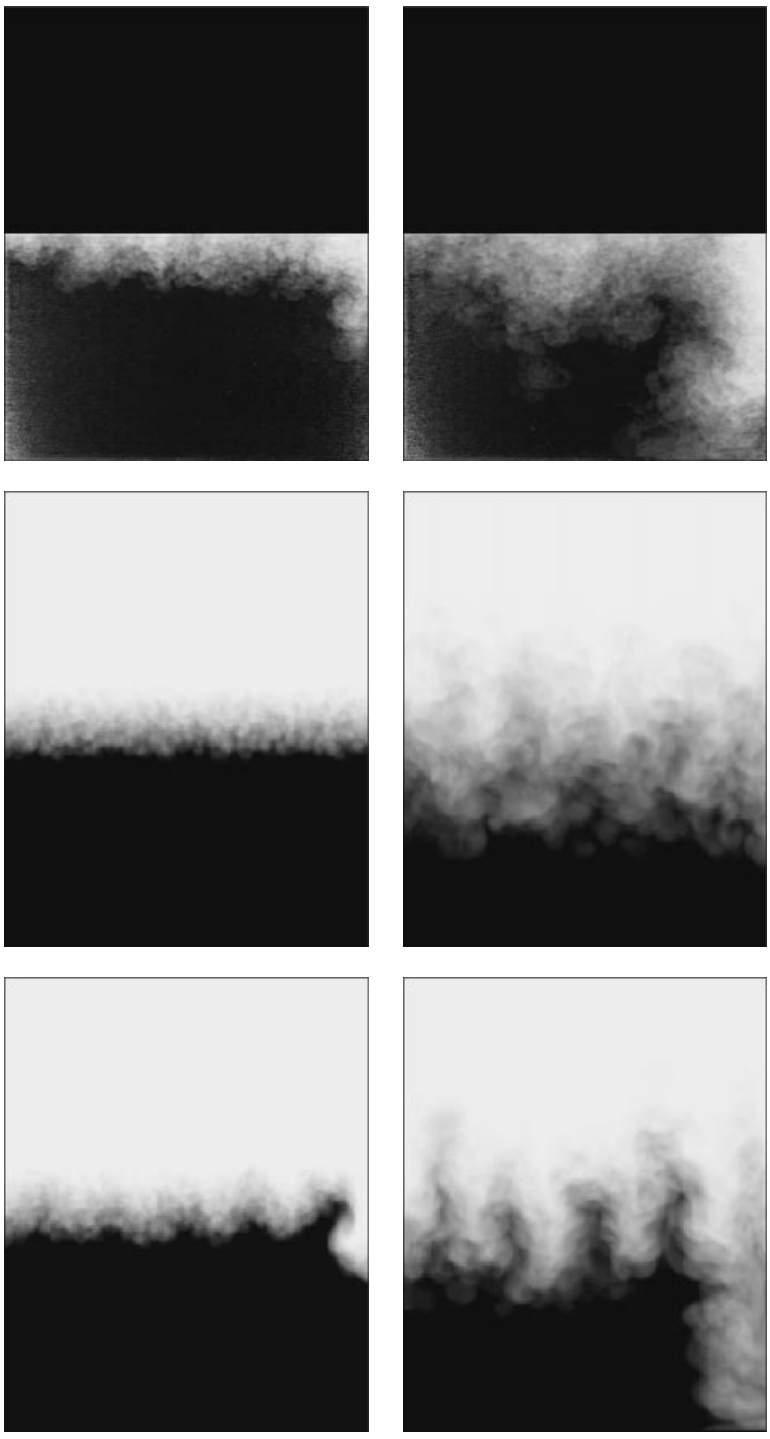

FIGURE 8(*a*, *b*). For caption see facing page.

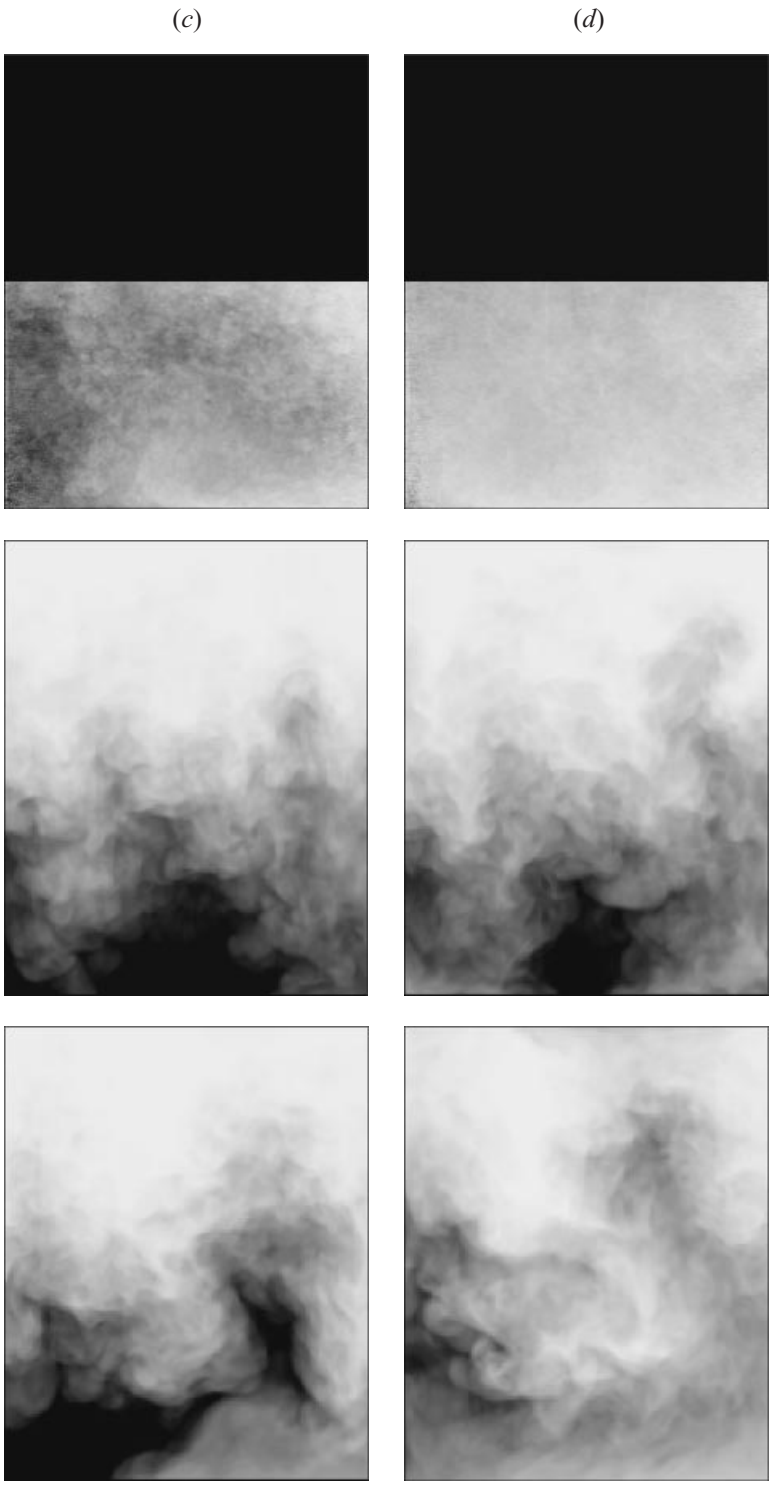

FIGURE 8. As for figure 6, but showing the ensemble mean flow for the experiments and the cross-tank mean flow for the simulations.

tank. The fluid originating from the unprotected strip down each side of the barrier and entering the light sheet is again a consistent feature of the experiments not found in the simulations due to its absence in the initial conditions used for the simulations.

Some of the structure found in the individual slices for the idealized simulations persists in the cross-tank mean. As early as $\tau = 2$ (figure 8*b*) there is evidence of some structure in these means related both to the initial noise (introduced to trip the instability) and its coupling with the tank walls. It has often been stated that idealized Rayleigh–Taylor instability loses its memory of the initial conditions, but this is only true in a statistical sense. Taking the planar concentration mean recovers the up/down symmetry expected in this low Atwood number flow. Similarly, taking an ensemble mean of idealized simulations initiated with a different set of random modes effectively eliminates this structure.

4.2. *Perspective views*

Figures 9 and 10 show perspective views of the early stages in the developing experimental and simulated flow. These views are included to give a qualitative impression of the three-dimensional character of the instability.

Two views of the same experiment are shown in figure 9. The left-hand column shows the flow viewed through the endwall at an angle of approximately 30° to the horizontal, while the right-hand column views the flow looking down through the floating lid at approximately 60° above the horizontal. The orientation of these views is sketched in figure 1. In both cases only the right-hand 30% of the tank is visible, with the barrier being withdrawn towards the viewer. Note that this experiment was conducted with $A = 0.0007$ compared with the $A = 0.002$ used for the other experiments reported here. This has little effect other than to increase the characteristic time scale from 5 s for the basic $A = 0.002$ flow to 8.5 s for the lower Atwood number flows.

The flow soon after the passage of the barrier contains a significant two-dimensional component clearly visible in the top view of figure 9(*a*) but which is not apparent in the end view. The rapid downward motion adjacent to the right-hand endwall (the far end in these perspective views) is difficult to discern, even when viewing the original video footage (for practical reasons it was not possible to dye the upper layer to obtain perspectives from below in which this plume would be clearly visible). The two-dimensionality of the initial structure soon becomes less apparent as the three-dimensional instability takes over. These perspective views highlight the smaller dominant length scales so that while there is still a significant two-dimensional component present at $\tau = 0.5$, it is no longer visible in either view of figure 9(*b*).

The upward-propagating bubbles of light fluid are remarkably smooth, especially when contrasted with the presence of the very fine scales seen in the LIF images of figure 6. This smoothness is not simply an artefact of the method of visualization, but the result of the intense divergence of the dense fluid pushed aside by the rising bubble. This divergence causes any fine-scale features swept away from the nose of the bubble to be accumulated in the wake behind. Not all of the structures visible in the LIF images in figure 6 show such smooth leading-edge geometry as for many of these bubbles the light sheet is not aligned with the flow but instead cuts through the structures at locations where there is no strong divergence.

The number of mushroom-like structures decreases rapidly as their length scale grows. While some small structures continue to exist between the largest structures, they are increasingly engulfed by the growing dominant scale. The end views show clearly that this process occurs in a uniform manner across most of the width of

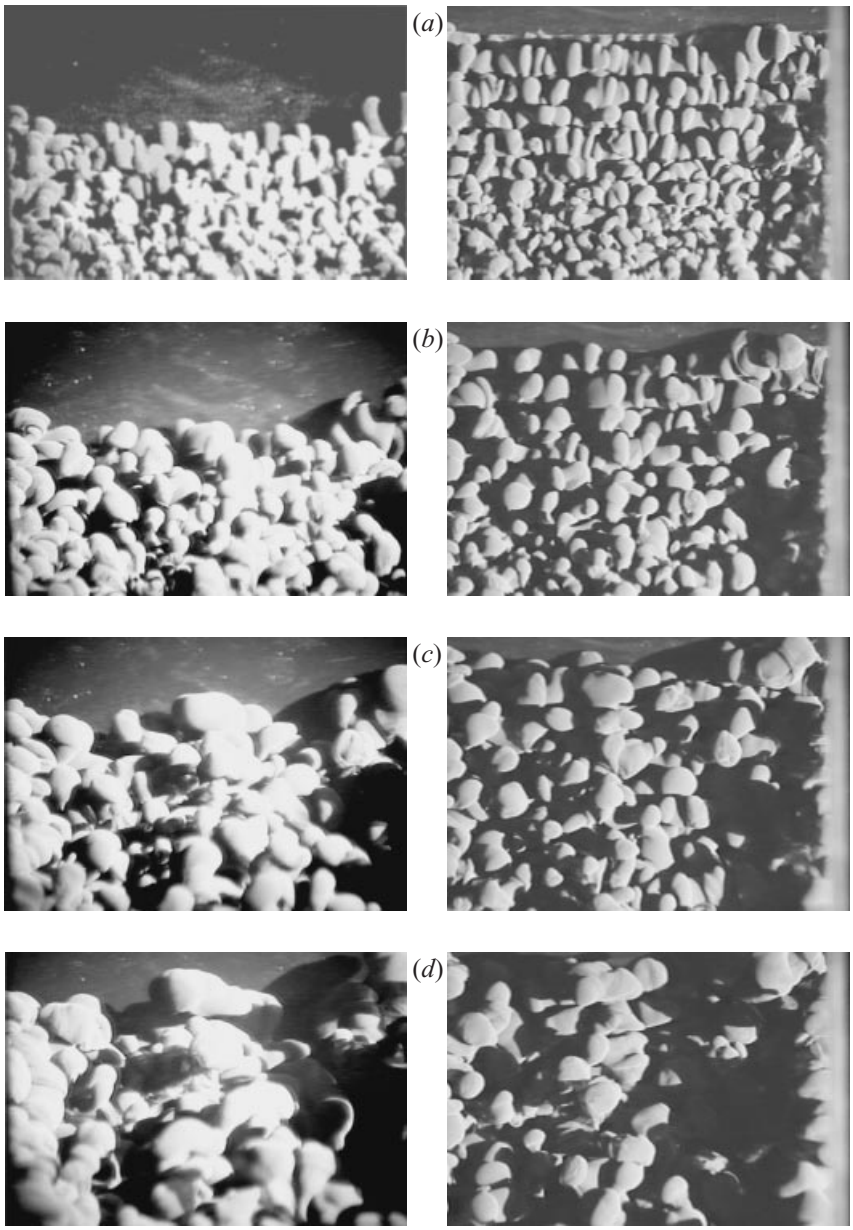

FIGURE 9. Perspective views of the early stages of development of the instability for an $A \approx 7 \times 10^{-4}$ flow. The left-hand column shows the view through the endwall of the tank and the right-hand column the view through the floating lid on the top of the tank. The same experiment is shown for both views at times (*a*) $\tau = 0.25$ ($t = 2.12$ s), (*b*) $\tau = 0.5$ ($t = 4.24$ s), (*c*) $\tau = 0.75$ ($t = 6.36$ s), and (*d*) $\tau = 1.0$ ($t = 8.48$ s).

the tank. The exception to this uniform growth is the flow immediately adjacent to the front and back walls (right and left side of the perspective views) where the flow generated by the unprotected strip down either side of the barrier is just visible. Interaction between this flow and the interior of the tank appears to be confined largely to the area immediately adjacent to the walls until this flow starts to interact with the top and bottom of the tank. The sequence is terminated after $\tau = 1$ because

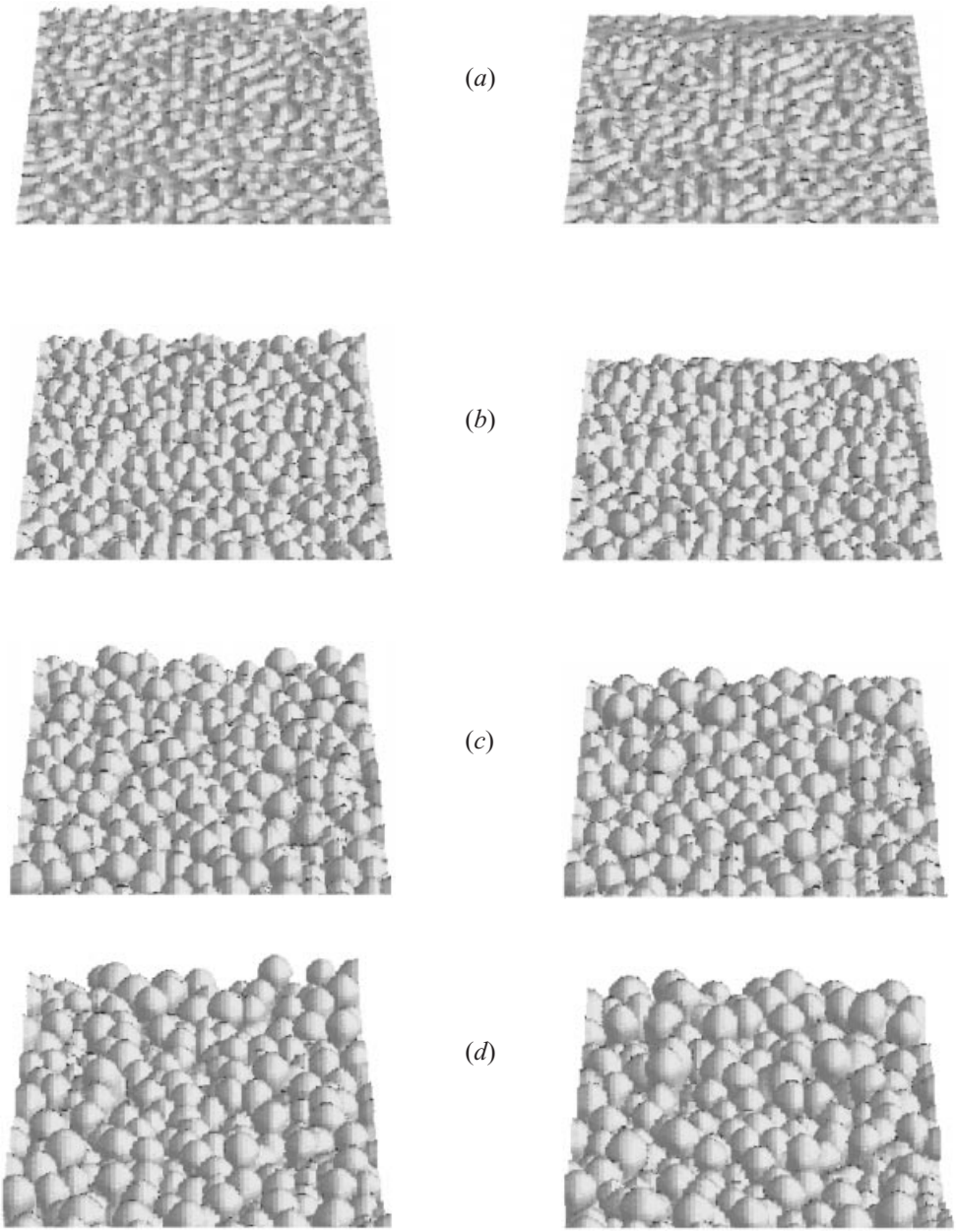

FIGURE 10. Perspective views from the simulations. Idealized initial conditions are shown in the left-hand column and simulations initialized with experimental initial conditions are shown in the right-hand column. Views are for the same times as in figure 9: (*a*) $\tau = 0.25$, (*b*) $\tau = 0.5$, (*c*) $\tau = 0.75$, and (*d*) $\tau = 1.0$.

the mixing zone extends beyond the field of view of the video camera and shadowing of the interior of the flow by the more rapid growth above these unprotected strips.

Perspective views of the idealized and barrier simulations are shown in figure 10 with approximately the same orientation and perspective as the end views of the experiment in figure 9. Visually the two simulations appear very similar and both contain a more

homogeneous array of structures than found in the experiments, but there is less detail available, partly due to the limited resolution of the simulations, and partly due to the method of rendering the $C = 0.975$ iso-concentration surface. The initial length scales of the developing three-dimensional structures are, if anything, slightly larger than those seen in the experiments. As this length scale is imposed by the random component of the initial conditions, it suggests that the three-dimensionality of the experiments contains more power at the higher wavenumbers. The less homogeneous character of the experimental structures is due in part to evolution during the withdrawal process, and in part to the wider range of scales excited by the barrier than have been modelled for the numerical simulations.

The superimposed two-dimensional barrier perturbation is just discernible in the barrier simulations (figure 10*b*, right-hand column), more through its modulation of the random component than by being visible directly. The slower growth rate for the idealized simulations is also detectable, although it does not stand out clearly.

5. Mixing zone growth

The growth of the mixing zone has received more attention in the literature than any other single measure of the development of the instability. In this section we first introduce the definition of the width of the mixing zone used by a selection of the previous researchers and compare the results obtained in this way for the current experiments and simulations. After considering the limitations of this definition, a number of alternative definitions are explored and their results compared.

5.1. *Growth rate*

A precise definition of the length-scale of penetration of one layer into the other has often been lacking, especially in the experimental context. For simulations some degree of consistency has been enforced, at least for individual researchers, through the need to utilize a program to extract the data from the simulations, but experimental measurements have often been done by eye with differing criteria from image to image and experiment to experiment. With the experimental LIF images now available in a digital format, it is possible to remove the subjective element of this analysis. Furthermore, by converting the simulation output into virtual images, all three data sets may be analysed in exactly the same manner with the image processing software.

The most widely used definition of the mixing zone width has been based on the plane-averaged concentration profile. In particular, the width is defined as the depth at which this profile reaches a prescribed threshold concentration level, C_1 (say).

For this paper we use an overbar to indicate along-tank averaging such that $\overline{C(z,t)}$ represents vertical profiles of the along-tank mean of the concentration field of a single experimental realization or a single along-tank vertical plane of data from the simulations. While these profiles could be used to compute h_2 by finding $\overline{C(z = h_2, t)} = C_1$, these data would be subject to significant statistical fluctuations from one experiment or data plane to the next. In order to reduce these fluctuations and reduce the sensitivity to a single experiment for the initial conditions in the barrier simulations, we employ ensemble as well as spatial averaging to construct the profiles. In particular, the experimental $\overline{C(z,t)}$ profiles are averaged over 16 realizations (cross-tank averages are not employed due to the effects of the unprotected strip down either side of the tank). With the idealized simulations the $\overline{C(z,t)}$ profiles are averaged across the width of the tank (effectively recovering a planar average profile), while for the barrier simulations a combined planar and ensemble averaging (over

three realizations) is employed. Thus the concentration is averaged over the largest data sets possible to compute the vertical profile. We use the notation $\langle \bullet \rangle$ to represent data which have been averaged over an ensemble and/or the width of the tank. Hence $\langle \overline{C(z,t)} \rangle$ represents the ensemble average of $\overline{C(z,t)}$ for the experiments, the planar average concentration profiles for the idealized simulations and the combined planar and ensemble average for the barrier simulations.

Figure 11 presents the vertical profiles of the planar/ensemble-average concentration as a function of time. These $\langle \overline{C(z,t)} \rangle$ profiles are rendered as a greyscale which, to aid interpretation, varies as $aC + b\cos(10\pi C)$ to produce a sequence of light and dark bands. The superimposed curves represent the quadratic growth law (3) with $\alpha_i = 0.03$, 0.05 and 0.07, $i = 1, 2$.

As only the flow in the lower half of the tank was visualized, the experimental data are missing for the upper half of the tank. Further, during the first 2 s of the experiments, the barrier remained visible in the field of view, contaminating the $\langle \overline{C(z,t)} \rangle$ profiles in figure 11(*a*) near $z = 0$. Comparison with the superimposed quadratic curves shows the results are in broad conformity with the similarity law, but not in close agreement. The idealized simulations in figure 11(*b*) show a lower growth rate and much closer agreement, while the barrier simulations (figure 11*c*) follow the same trends as the experiments.

The superiority of the barrier simulations for modelling the flow can be analysed by considering scatter plots of the $\langle \overline{C(z,t)} \rangle$ concentrations and the correlation coefficient between the respective data sets. Figure 12 presents these scatter plots as greyscale images, where the darkness of the greyscale represents the frequency of the relationship. There is clearly less structure in the scatter plot between the experiments and idealized simulations (figure 12*a*) than is found between the experiments and barrier simulations (figure 12*b*), particularly at the lower concentrations which mark the downward propagation of the mixing zone. For the idealized simulations correspondence between the two concentration profiles is found only for the highest concentrations which occur near $z = 0$, $t = 0$, whereas the barrier simulations show a clear functional relationship for all time and space. The correlation coefficients are 0.82 and 0.62 for figures 12(*a*) and 12(*b*), respectively.

Linden *et al.* (1994) and Dalziel (1993) have both presented fits for h_2 where $\langle \overline{C(z = h_2, t)} \rangle = C_1$ for some threshold concentration C_1. In an attempt to modify the similarity law to make some allowance for the non-ideal initial conditions imparted by their respective barriers, Linden *et al.* (1994), who estimated the penetration by eye, assumed the penetration to start from some time origin $t_0 < 0$. Dalziel (1993), measuring the penetration from digitized images (but without the corrections applied in the data sets presented here), allowed the addition of a linear term to the growth. The data presented here could be treated in a similar manner. Linden *et al.* (1994) commented that it was difficult to obtain an unambiguous value for α_i, and Dalziel (1994*a*) showed the value of α_i obtained from a formalized fitting procedure depends on the number of terms fitted and the temporal range of the data used. While their precise forms differed, the net effect was similar, and any attempt to fit a quadratic dependence to the data in a systematic manner would lead to a potentially large range of viable values for α_1 and α_2. The same arguments apply here to the experimental data and the barrier simulations.

There are two related reasons for the inconsistency of quadratic fits to the experimental and barrier simulation $\langle \overline{C(z,t)} \rangle = C_1$ data sets. First, the growth from the finite perturbations produced by the removal of the barrier is not simply the sum of linear and quadratic terms for the time dependence and, second, the flow does not have

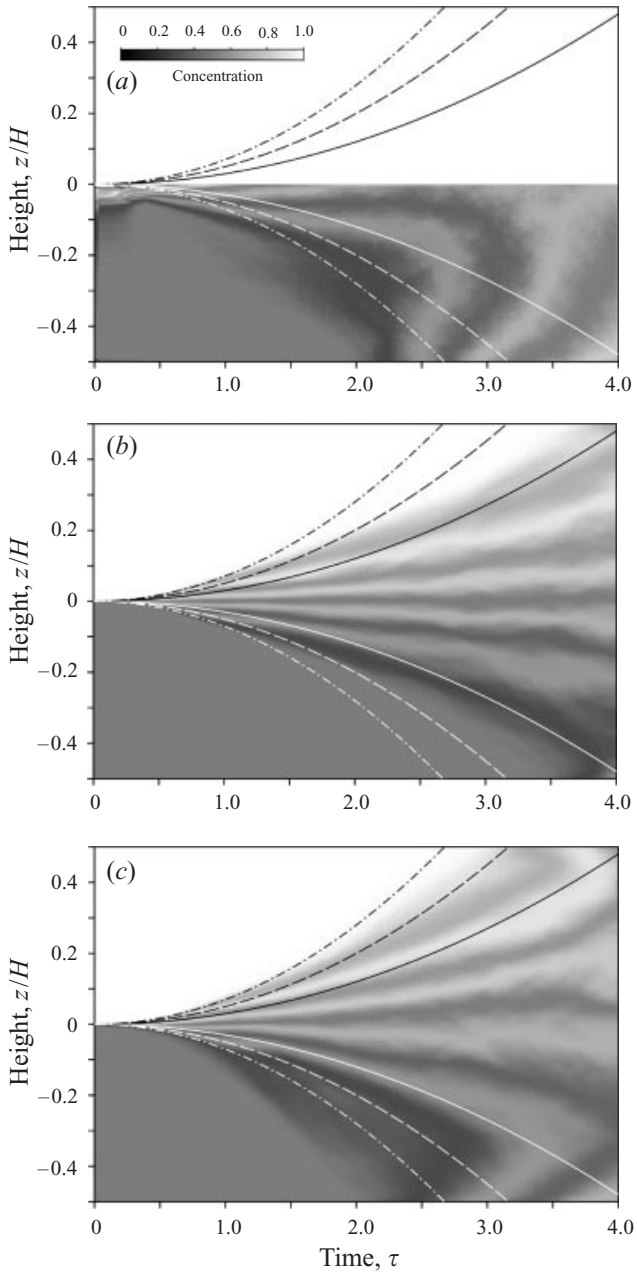

FIGURE 11. Evolution of profiles of the mean concentration field. (*a*) The experimental data, averaged over the length of the tank and over the 16-experiment ensemble. The simulations with (*b*) idealized initial conditions and (*c*) the measured initial conditions. For the simulations the data are averaged over the length and width of the flow domain. The superimposed curves represent the quadratic growth of the similarity law with values of $\alpha_i = 0.03$, 0.05 and 0.07 ($i = 1, 2$) for the solid, dashed and dot-dashed lines (respectively).

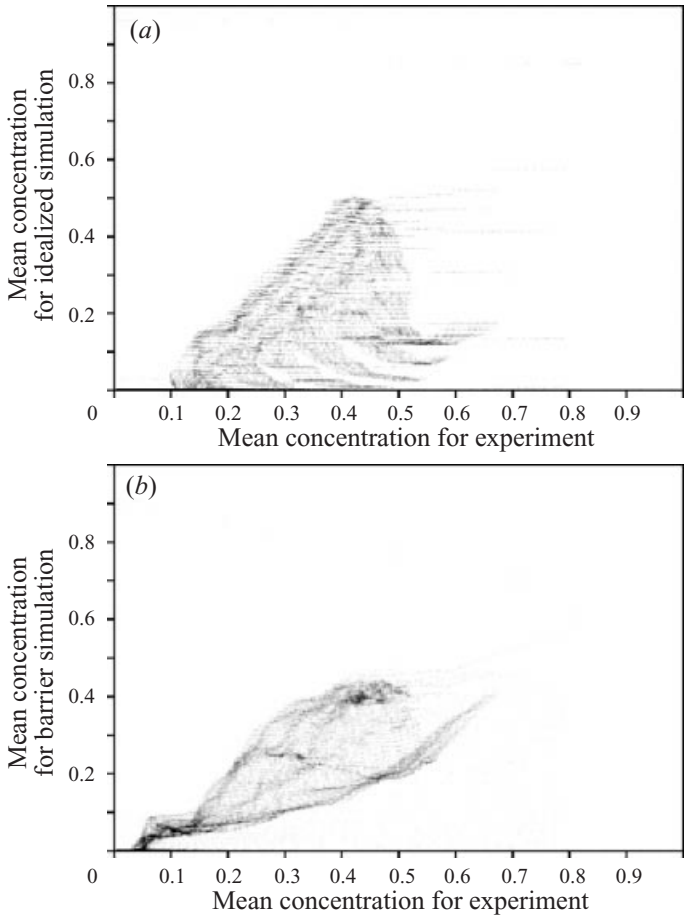

FIGURE 12. Scatter plot of $C(z,t)$ between (a) experiments and idealized simulations, and (b) experiments and barrier simulations. In both cases the simulations occupy the vertical axis and the experiments the horizontal. The frequency of the relationship is represented as a greyscale.

the horizontal homogeneity implicit in the similarity law. The barrier perturbations, whether the simple solid barrier of Linden *et al.* (1994), or the composite barrier of Dalziel (1993) and the present study, both introduce additional (horizontal) length scales at $t = 0$. Not only do these length scales have their own time scales associated with them, but they represent different dynamics in different regions of the tank.

In contrast, the idealized simulations are well-modelled by quadratic time dependence, as found by earlier investigators. The values of α_1 and α_2 here are both ~ 0.04, consistent with those reported by Youngs (1994*a*) and Linden *et al.* (1994). With only a small-amplitude initial random perturbation to the interface position to trigger the instability, the quadratic growth is achieved almost immediately. Similar results have been found when the small-scale random perturbation is applied to the velocity field rather than the interface position. Linden *et al.* (1994) showed that the introduction of a long-wave perturbation delays the start of the similarity phase of the growth.

In an attempt to remove, or at least reduce, the influence of the plume down the right-hand end of the tank, figure 13 presents the $\langle \overline{C(z,t)} \rangle$ data sets for the flow in the left-hand half of the tank for the experiments and barrier simulations.

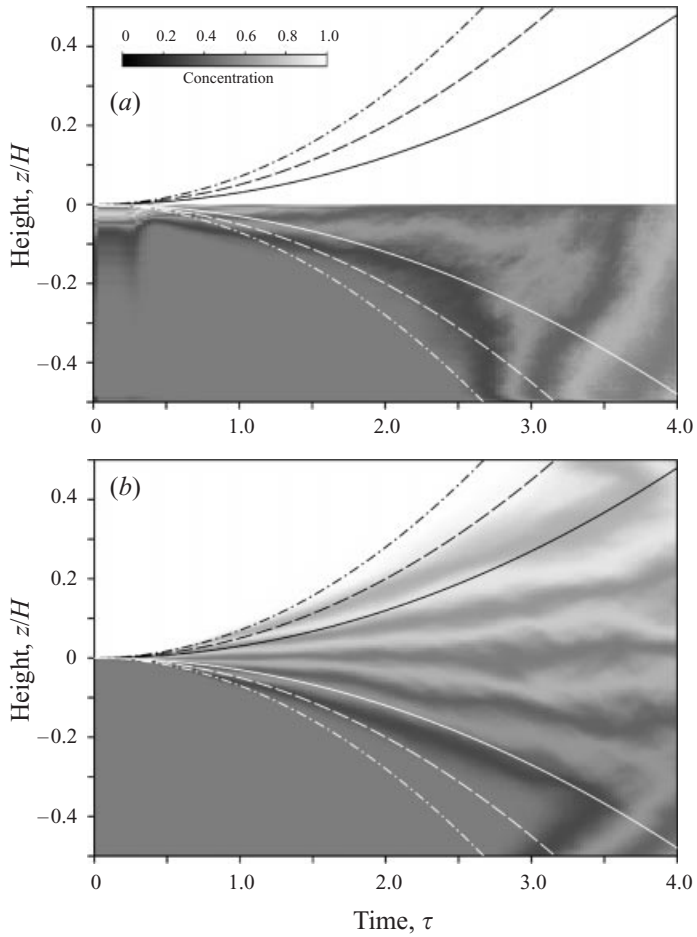

FIGURE 13. As for figure 11, but showing the mean profiles for the left-hand 50% of the length of the tank for (*a*) the experimental data and (*b*) the barrier simulations.

The corresponding plot for the idealized simulation is essentially the same as that presented in figure 11(*b*) due to the more homogeneous nature of this flow. Again the experiments and barrier simulations are in close agreement with a lower growth rate than was found for the entire length of the tank. Arguably this growth is modelled more closely by the simple quadratic time dependence, at least up until the mixing zone first reaches the floor of the tank. The agreement between the two deteriorates after this point due to the effect of the unprotected strips down either side of the barrier. The combination of this un-modelled flow plus the gravity current propagating across the floor lead to a departure from the quadratic law.

5.2. *Integral measures*

As an alternative to the penetration measured by thresholding the mean concentration profiles, Youngs (1994*b*) suggested using the integral mixedness

$$h_{Integral} = \int_{-H/2}^{H/2} \langle \overline{C} \rangle (1 - \langle \overline{C} \rangle) \, \mathrm{d}z, \tag{6}$$

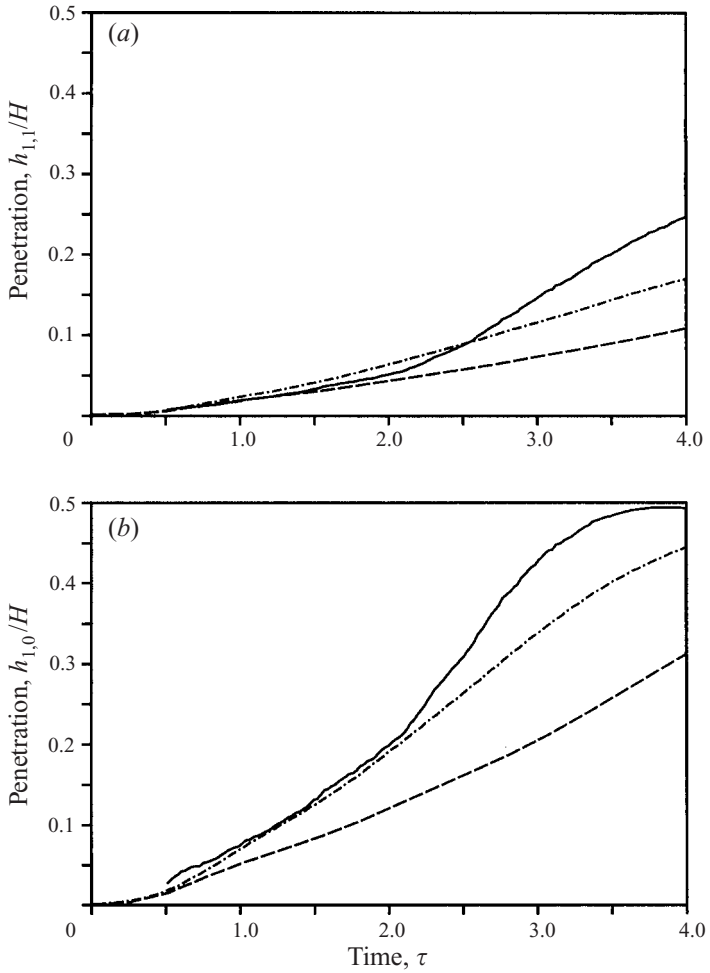

FIGURE 14. Integral measures for the growth of the mixing region: (*a*) $h_{1,0}$ and (*b*) $h_{1,1}$. The experimental data are shown as solid lines, the simulations with idealized initial conditions as dashed lines and the simulations using experimentally derived initial conditions with dot-dash lines.

as a more robust measure, less susceptible to statistical fluctuations than h_2. Both the similarity law and the results presented by Youngs suggested $h_{Integral}$ should also follow a quadratic growth. Dalziel (1994*b*) adapted this to consider the lower half of the tank only and extended the possible measures to include

$$h_{m,n} = \frac{(m+n)^{m+n}}{m^n n^m} \int_{-H/2}^{0} \langle \overline{C} \rangle^m (1 - \langle \overline{C} \rangle)^n \, \mathrm{d}z, \tag{7}$$

where m and n are integers. The factor outside the integral has been introduced to limit $h_{m,n}$ to the range $[0, H/2]$. For the present paper we shall consider only $h_{1,0} = \langle \overline{C} \rangle H/2$, the amount of upper-layer fluid in the lower half of the tank, and $h_{1,1}$ which, for a symmetric density field, is $2h_{Integral}$.

Figure 14 plots these integral measures for the experiments and simulations. The plane and ensemble averaging to obtain $\langle \overline{C(z,t)} \rangle$ for these calculations is identical to that employed in figure 11. The three curves in figure 14(*a*) give the $h_{1,0}$ measure of the

penetration. The corresponding curves in figure 14(*b*) are for the integral mixedness, $h_{1,1}$. Both sets of curves follow an approximately quadratic increase with time up to $\tau \approx 2$ when the mixing zone extends to the bottom of the tank. The experimental curves remain in close agreement with the barrier simulations until $\tau \approx 2.5$ at which time fluid originating from the unprotected strips down either side of the barrier enters the field of view.

After $\tau \approx 2.5$ it is clear that the experiments become more efficient at transporting dense upper-layer fluid to the lower half of the tank due to the strength and coherence of the large-scale overturning motion. The integral mixedness reaches a maximum at $\tau \approx 3.5$ with the mean concentration of upper-layer fluid increasing through 0.5 ($z/H = 0.25$) as the stable stratification becomes established.

Similar measurements with the averaging restricted to the left-hand half of the tank show the importance of the flow down the right-hand wall, with the experiments and barrier simulations again in good agreement up to $\tau \approx 2.5$. In this restricted data set the values of $h_{1,0}$ and $h_{1,1}$ are substantially lower than those based on the whole length of the tank and, for $\tau \lesssim 1.5$, are comparable with those for the idealized simulations. This is a result of the weak upward flow resulting from the barrier perturbation reducing the apparent local growth rate into the lower layer. The rate of growth of the mixing zone into the upper layer is, of course, enhanced by this flow in the left-hand half of the tank.

The growth from the idealized simulations (dashed curves) is substantially lower than the experiments or barrier simulations. The curves for the idealized simulations are, as expected, identical whether the averaging is over the entire length of the tank or the left-hand end only. Compared with the experimental data and barrier simulations, we find a lower growth rate for an average over the entire length of the tank, repeating our earlier findings. As may be expected from the similarity law, the $h_{1,0}$ curve is well fitted by τ^2 until the mixing region extends to the bottom of the tank. The $h_{1,1}$ curve is less well-modelled by a quadratic growth law for $\tau \lesssim 1$, reflecting the initial growth phase before the flow becomes fully nonlinear.

6. Structure within the mixing zone

We have seen in the previous section that for external measures of the instability, such as the width of the mixing zone, the experiments agree well with the barrier simulations, but there is only poor agreement with the idealized simulations. In this section we look in more detail at the internal structure of the developing instability to establish how this is affected by the barrier-induced perturbation and how well the barrier simulations model the experiments in these features. The estimates of the fractal dimension given here are more accurate than those reported by Linden *et al.* (1994). Moreover, concentration power spectra have been measured for the first time for Rayleigh–Taylor instability.

6.1. *Power spectra*

Concentration power spectra provide not only details of the mixing between the two fluid layers, but, by inference, also provide details of the state of the turbulence produced by the instability. We focus on the along-tank concentration power spectra and average the results over the region $-0.1 \leqslant z/H \leqslant 0$ just below the initial density discontinuity. As with the results presented in the previous section, the experimental spectra were averaged over the ensemble of sixteen runs while the idealized simulations

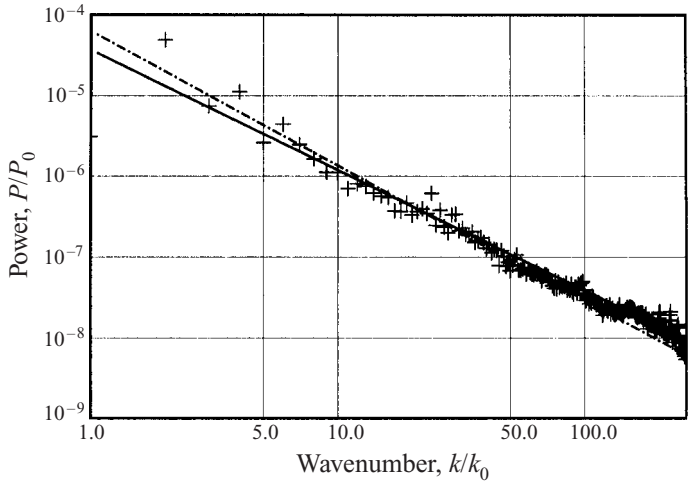

FIGURE 15. Typical horizontal concentration power spectrum from the ensemble of 16 experiments. The spectrum is shown for $\tau = 2$ and is calculated over a window extending from $z/H = -0.1$ to $z/H = 0$. The + marks represent the arithmetic mean power level while the solid line is a weighted least-squares power-law fit to the data for dimensionless wavenumbers in the range $10 \leqslant k/k_0 \leqslant 50$. The dot-dashed line represents a $k^{-5/3}$ spectral slope.

were averaged over the width of the tank and the barrier simulations averaged over both the width of the tank and the three runs in the ensemble.

In the absence of a horizontally periodic domain, the data had to be continued or padded prior to computing their Fourier transform. For the results presented here the data (160 mesh points for the simulations and 492 pixels for the experiments) were extended to the next power of 2 using a linear interpolation between the concentrations at either end of the domain. A standard one-dimensional fast Fourier transformation algorithm was used to generate the power spectra prior to averaging. Trials with artificially generated data and comparison with other windowing strategies using a direct Fourier transformation algorithm confirmed the appropriateness of this approach. The averaging of the power levels was achieved using both arithmetic and geometric means and the results obtained compared and found to be in good agreement. As the arithmetic average is more easily interpreted theoretically, only these averages are presented here. The spectra from the experiments have also been calculated with different horizontal window sizes. These tests have shown the spectral slopes to be insensitive to the size and position of the window, and to the poor signal-to-noise ratio in the left-hand side of the images. Spectra based on the whole length of the tank are presented here as these provide the largest self-similar range and the least contamination by the padding and windowing procedure. We are interested primarily in the spectra for length scales small compared to the length of the tank and so any weak contamination by the windowing and padding procedure is not important. Moreover, at these wavenumbers the one-dimensional spectra calculated here yield the same wavenumber dependence as integrating three-dimensional spectra over spherical wavenumber shells (Tennekes & Lumley 1972, p. 253).

Figure 15 shows the arithmetic ensemble mean power spectrum for the experiments at $\tau = 2$. A weighted least-squares power-law fit to the data in the range $10 \leqslant k/k_0 \leqslant 50$, where $k_0 = 2\pi/L$, is shown as a solid line. This range of wavenumbers was selected in order to avoid contamination by the large-scale motions introduced by the barrier

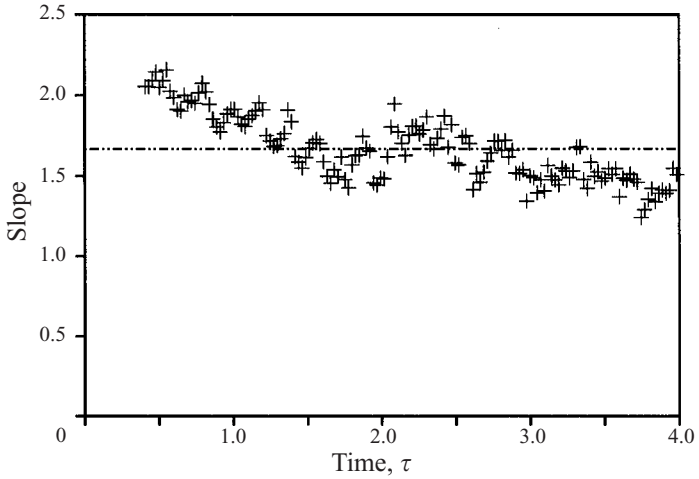

FIGURE 16. The time evolution of the spectral slope, as determined by least-squares fits to the spectral data of the type shown in figure 15, for the ensemble of experiments.

at the small-wavenumber end, and the signal noise at the high-wavenumber end. The choice also effectively eliminates any influence from the procedure to extend the data. The slope of this line is -1.49. The departure from the power-law behaviour for wavenumbers $k/k_0 > 128$ is due primarily to pixel noise in the processed images. This cut-off corresponds approximately to the Kolmogorov length scale beyond which we would expect a flattening of spectra for this high-Schmidt-number flow. The power levels have been normalized by P_0 such that $P/P_0 = 1$ at $k = 1$ for a uniform concentration $C = 1$.

A wide variety of fully developed turbulent flows display the $k^{-5/3}$ Kolmogorov velocity spectrum (Tennekes & Lumley 1972, p. 263), a characteristic common in both experimental and numerical studies. Moreover, a scalar field, initially distributed in a smooth manner, will be advected by the same turbulence to give a concentration field with the same wavenumber dependence (Tennekes & Lumley 1972, p. 283). The dot-dashed curve in figure 15 shows that for the present Rayleigh–Taylor instability a $-\frac{5}{3}$ slope is consistent with the experimental measurements. Arguably this fit is as appropriate as the more general power-law fit (which is sensitive to the precise range of data and weighting function used) discussed above, and shows the concentration fields to be consistent with a Kolmogorov velocity spectrum.

The spectra for individual realizations agree well with the ensemble mean, showing only a slight difference in slope and increased scatter. Changing the vertical extent over which the power is averaged impacts the scatter more than the slope. Extending this region to include the entire lower half of the tank leaves the mean almost unchanged except at very small wavenumbers.

Figure 16 shows the time evolution of the spectral slope, where the slope was evaluated using the same weighted least-squares routine used for the fits in figure 15. For $\tau > 0.4$ the slopes decrease from around 2 to the $\frac{5}{3}$ value indicated by the horizontal line. Examination of the individual spectral plots suggests the degree of scatter in the slope reflects the scatter in the individual plots and that the true spectral slope is changing only on an $O(1)$ time scale. The steep k^{-2} slope at early times ($\tau \lesssim 1$) is due to the combination of the energy introduced at relatively large scales by the withdrawal of the barrier, and the time required to establish fully developed

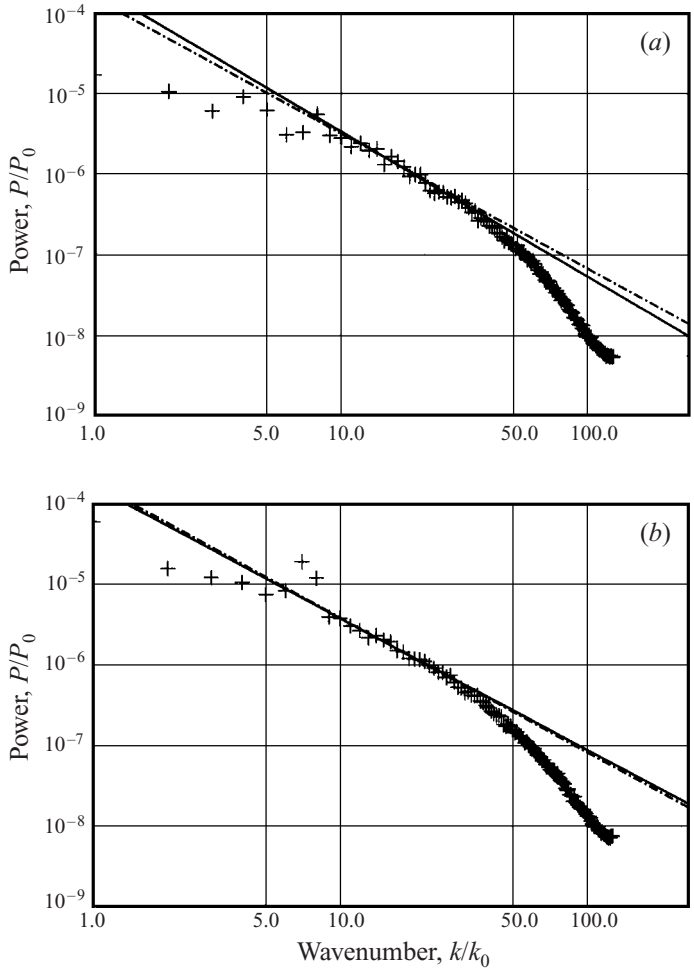

FIGURE 17. Typical horizontal concentration power spectra from the numerical simulations using (*a*) idealized initial conditions and (*b*) experimentally derived initial conditions. In both cases the spectra are shown for $\tau = 2$, and are calculated over a window extending from $z/H = -0.1$ to $z/H = 0$ using arithmetic averaging over the width of the tank. The solid line is a weighted least-squares power-law fit to the data for dimensionless wavenumbers in the range $10 \leqslant k/k_0 \leqslant 25$. The dot-dashed line represents a $k^{-5/3}$ spectral slope.

turbulence. This view is reinforced by examination of the individual spectra at these early times which show that a much smaller range of wavenumbers follow a power law than found at $\tau = 2$ in figure 15.

The decrease in spectral slope for $\tau > 3$ occurs when the mixing zone has extended to fill the entire tank and a globally stable stratification is established. In these conditions, the large length scales are affected by the globally stable nature of the stratification, while the smaller length scales are influenced by the locally unstable regions. As a result the large length scales are damped by the stratification, with their energy being transferred to the density field in the form of internal waves, leading to a decrease in the spectral slope since the smaller scales are not damped as efficiently. Even if the locally unstable regions were not present, the larger scales would be damped preferentially by the stratification.

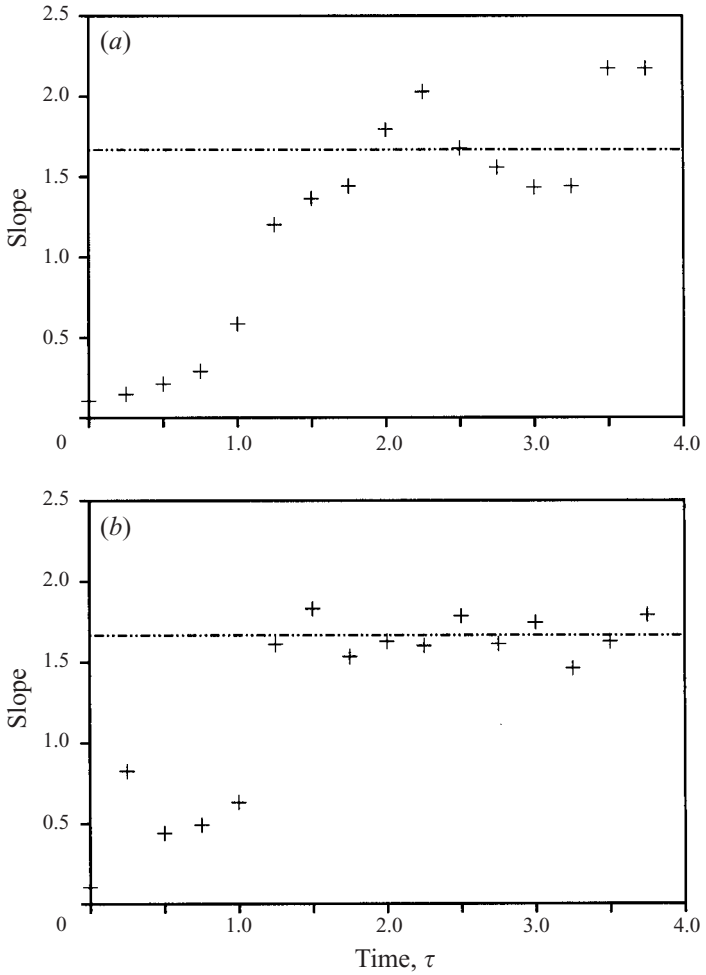

FIGURE 18. The time evolution of the spectral slope for the simulations using (*a*) idealized initial conditions and (*b*) experimentally derived initial conditions, calculated as for the experimental data shown in figure 16.

Figure 17 plots the mean spectra at $\tau = 2$ for the idealized (figure 17*a*) and barrier (figure 17*b*) simulations. Weighted least-squares power-law fits to the data in the range $10 \leqslant k/k_0 \leqslant 25$ are indicated by solid lines, with the dot-dashed line signifying a $k^{-5/3}$ spectrum. The use of a smaller range of wavenumbers to determine the spectral slope reflects the reduced range over which a power-law relation may be found and the lower resolution of the numerical concentration fields.

The fitted power-law relationships give slopes of -1.79 and -1.63 for the idealized and barrier simulations, respectively. The data show significant curvature even within the $10 \leqslant k/k_0 \leqslant 25$ range used to establish the spectral slope. Comparison with a $k^{-5/3}$ relationship suggests this would also be a reasonable fit to the spectra. The roll-off at high wavenumbers is an artefact of the finite resolution and numerical diffusion of the simulations combined with the $O(1)$ Schmidt number for the simulations. Earlier work with the same numerical model (Linden *et al.* 1994) shows that for homogeneous turbulence, the velocity power spectra are well fitted by $k^{-5/3}$ down to a wavelengths

of $6\Delta x$, here corresponding to $k/k_0 \approx 26$, with the decay again increasing at higher wavenumbers.

Comparison of the power levels shows close agreement between the idealized and barrier simulations over most of the wavenumber range, with the largest differences occurring at the lowest wavenumbers where the flow is influenced most by the barrier-induced initial conditions. In contrast the experimental power levels are lower than the simulations by as much as a factor of 3 at low wavenumbers, and higher by a comparable factor at high wavenumbers. This variation reflects in part the broader range of wavenumbers giving power-law behaviour plus the higher resolution of the experiments providing more power at the highest wavenumbers.

The evolution of the spectral slope for the idealized and barrier simulations is plotted in figure 18. The idealized simulations (figure 18*a*) take much longer to establish the $k^{-5/3}$ spectrum indicative of fully developed turbulence, reflecting the slower growth rate for the instability, and the manner in which the initial disturbances were confined to $20 \leqslant k/k_0 \leqslant 40$ and extend to higher and lower wavenumbers only through nonlinear interactions.

The barrier simulations are initiated with a much broader range of length scales through the combination of the $20 \leqslant k/k_0 \leqslant 40$ random three-dimensional perturbation used for the idealized simulations, and the $1 \leqslant k/k_0 \leqslant 10$ two-dimensional model for the withdrawal of the barrier. In the barrier simulations the gap between these two ranges of wavenumber is filled by nonlinear interactions much more rapidly than the idealized simulations can extend to lower wavenumbers. As a result the $k^{-5/3}$ spectrum is established earlier in the barrier simulations, at $\tau \approx 1$, than the idealized simulations ($\tau \approx 1.8$).

Comparison of the barrier simulations (figure 18*b*) with the experimental (figure 16) spectral slopes shows that this initial development phase takes longer in the simulations due to the initial absence of scales in the range $10 < k/k_0 < 20$ and the absence of any three-dimensional motions for $k/k_0 < 20$. At late times ($\tau > 3$) the simulations do not show the trend towards a flattening of the spectra that was found in the experiments. There is some evidence to suggest this is due to a stronger stable stratification being set up earlier in the experiments. The weaker stratification in the simulations is due in part to the absence of the flow down the front and back walls caused by the unprotected strips along each side of the barrier and the order-unity Schmidt number.

6.2. *Fractal dimension*

The LIF visualizations of the experiments and the planar sections through the simulations both provide information on the intersection between iso-concentration surfaces and the viewed plane. Geometrically the intersection forms a set of contours in the viewed plane which may then be analysed using a variety of tools. The possible fractal geometry of such contours is one aspect which has received considerable attention in recent years. While much of the work has centred on plumes and jets (e.g. Lane-Serff 1993; Catrakis & Dimotakis 1996), Redondo & Linden (1990) have previously applied fractal analysis to Rayleigh–Taylor instability.

The present analysis differs from the work of Redondo & Linden (1990) in a number of ways. First, much higher resolution images could be used due to improvements in video technology and the introduction of propan2ol to the lower layer to remove the defocusing effect of refractive index variations. Second, a more powerful and better collimated light source enabled the thickness of the illuminated sheet to be of the same order as the Kolmogorov scale. Third, correction for the attenuation and divergence

of the light sheet enables iso-concentration rather than iso-intensity surfaces to be studied. Finally, the scope of the measurements has been greatly extended.

Both studies determine the fractal dimension as defined by Kolmogorov capacity using the box counting algorithm. The domain is divided into a set of touching but non-overlapping boxes characterized by size ε and the number of boxes $N(\varepsilon)$ through which the iso-concentration contour passes is counted. This number and the size of the boxes are related through the relationship

$$N(\varepsilon) \propto \varepsilon^{-D(\varepsilon)}, \tag{8}$$

where $D(\varepsilon)$ is the scale-dependent dimension. If this dimension is found to be independent of the scale, $D(\varepsilon) = D_2$ (say), the contour is said to be fractal.

Figure 19 presents the relationship between N and ε for the experiments (figure 19*a*), idealized simulations (figure 19*b*) and barrier simulations (figure 19*c*). In each case a clear power-law relationship is visible spanning two orders of magnitude of box size. The data presented here are for the $C = 0.5$ iso-concentration contour at $\tau = 2$ and the box counts have been averaged over the respective data sets. Individual realizations and data planes show the same degree of power-law behaviour, although there is some scatter in the slope. The fractal dimensions for each case are obtained by a least-squares fit to the data for box sizes $0.02 \leqslant \varepsilon/L \leqslant 0.2$, although the slopes so obtained are relatively insensitive to the precise range of data selected.

The data presented here are restricted to the central 50% of the length of the tank to avoid contamination by the poor signal-to-noise ratio on the left-hand side of the images. If the full length of the tank is included, this noise increases the calculated dimension by around 10%, whereas the results show relatively little sensitivity to the lower level of noise found in the central region. In contrast, this high-wavenumber noise had little impact on the power spectra presented in the previous section.

The time evolution of the fractal dimension for the $C = 0.5$ iso-concentration contour is shown in figure 20. All three flows are characterized by an initial growth in the dimension (which would be unity at $\tau = 0$ if the flow started from a perfectly flat interface), then an approximately constant dimension from $\tau = 0.5$. The differences during this initial phase reflect the differences in the initial conditions at the smaller scales. The two simulations exhibit a close similarity due to the same random three-dimensional perturbation being used for both, with only small differences resulting from the introduction of the two-dimensional barrier perturbation. The more vigorous three-dimensional nonlinear perturbations introduced by the real barrier lead to a more rapid initial growth in the fractal dimension.

The values of the dimension are in good agreement between $\tau = 0.5$ and $\tau = 2.2$. At around this time the flow from the unprotected strips down either side of the barrier enters the field of view and a globally stable stratification is established. As we have seen already with the power spectra, this implies that the energy in the larger length scales is reduced relative to that in the smaller scales. The iso-concentration contours begin to be smoother and more horizontal at larger length scales, although they remain as contorted as before at the finer scales. The net result is an increase in the fractal dimension due to the increasing dominance of the finer scales.

If the fluorescent dye used to mark the upper layer did not diffuse (but density did), and we were able to view an infinitely thin light sheet, then ultimately the stirring caused by the turbulent velocity field would lead to the iso-concentration contours covering an ever-increasing area until all motion had died away. The fractal dimension would increase towards 2 during this time, the limiting value depending on the Schmidt number for the flow. If the density also did not diffuse (i.e. the fluids

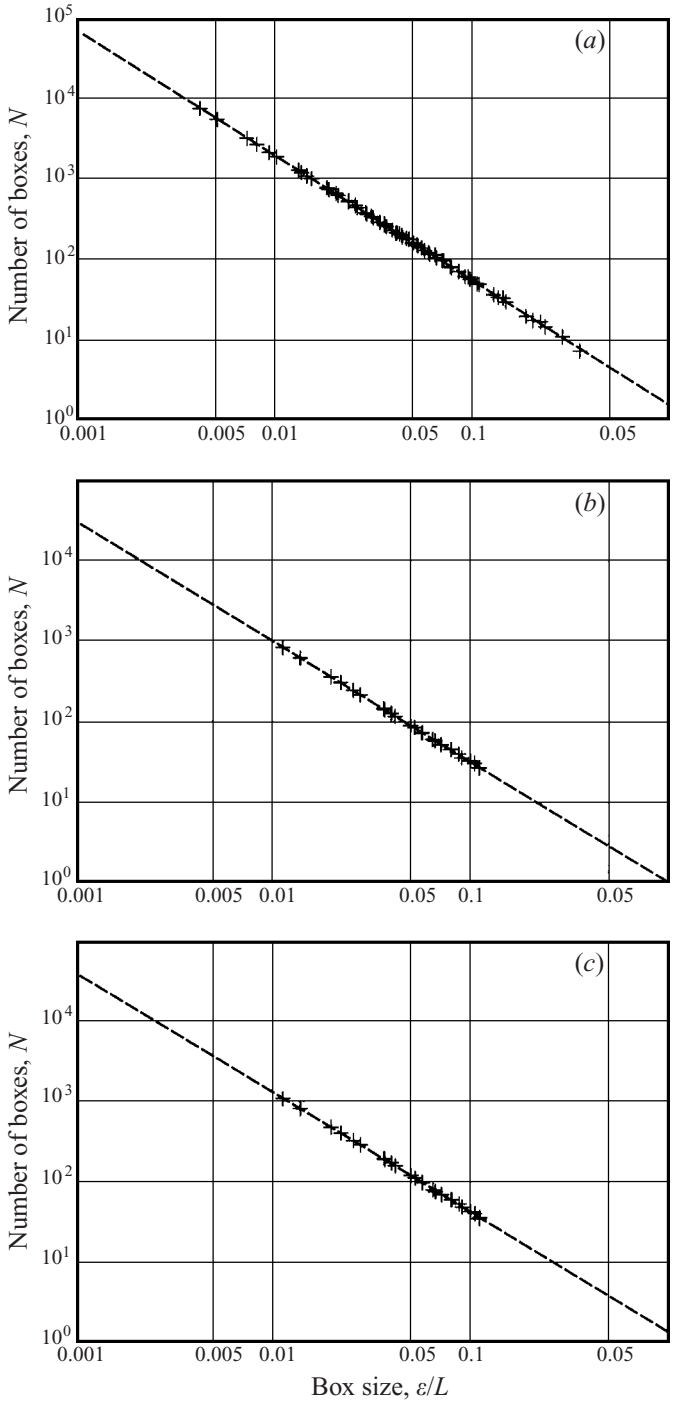

FIGURE 19. The power-law relationship between contour length and coverage using the box-counting algorithm. The plots shown are for $\tau = 2$ ($t = 10$ s) and the $C = 0.5$ concentration contour for (*a*) the experiments, (*b*) the simulations with ideal initial conditions and (*c*) the simulations using the barrier perturbation.

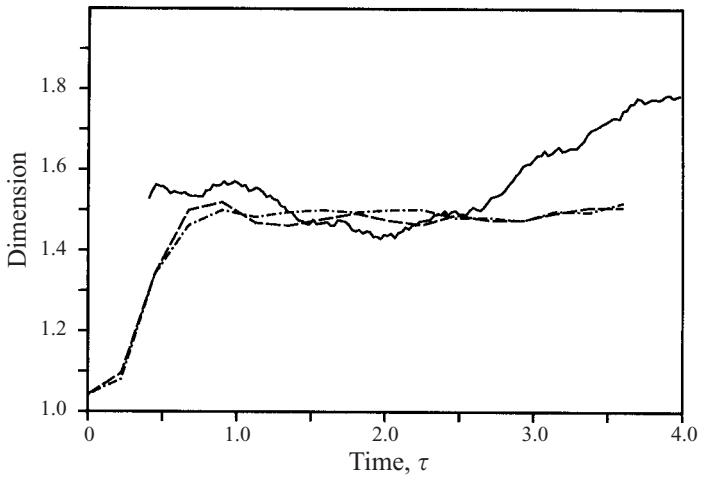

FIGURE 20. The time evolution of the $C = 0.5$ fractal dimension. The experimental data are shown with a solid line, the idealized simulations with a dashed line and the barrier simulations with the dot-dash line.

were immiscible), the dimension would tend towards unity as the fluids separated. For the experiments both density and the fluorescent dye diffuse so that, as the turbulence decays, the iso-concentration contours associated with the final stable stratification gradually become smoother and more horizontal, leading to a reduction in the fractal dimension. While the dimension is still increasing in the experimental data at $\tau = 4$, the curvature suggests that a maximum will soon be reached for the experimental data set. Calculation of the dimension at later times does show a reduction as will be seen in the time evolution of the dimension for lower concentration contours.

The concentration dependence of the measured dimension has also been investigated and the results plotted in figure 21. Curves are shown for $C = 0.5$ (solid), $C = 0.375$ (dashed) and $C = 0.25$ (dot-dash), and the dimension can be seen to be approximately independent of the concentration level selected up until $\tau \sim 2.2$. After this point the simulations remain independent of concentration, but the experimental curves diverge. As noted above, the increase in the experimental fractal dimension for $\tau \gtrsim 2.2$ results from the establishment of a globally stable stratification and the relatively slow diffusion of the fluorescent dye compared with the fluid momentum. This same Schmidt number effect combined with the vertical distribution of the density is the cause of the increased concentration dependence and eventual reduction in the fractal dimension in the experimental data.

The lack of concentration dependence in the fractal dimension for the present flows is in sharp contrast to the behaviour in plumes and jets. Concentration dependence has been found in plumes and jets to be the result of a strong correlation between the concentration and the intensity of the turbulence (e.g. Lane-Serff 1993). This intensity in turn reflects variations in the spatial and temporal structure of the flow. The fractal dimension is found to be higher for higher concentrations, which occur (on average) near the centreline of the plume or jet where there is a slower roll-off in the concentration power spectra. For the present Rayleigh–Taylor instability the turbulence is largely uncorrelated with the mean concentration field, at least where concentration fluctuations exist. In particular, the shape of the horizontal power spectra is observed to be independent of the vertical location within the mixing zone.

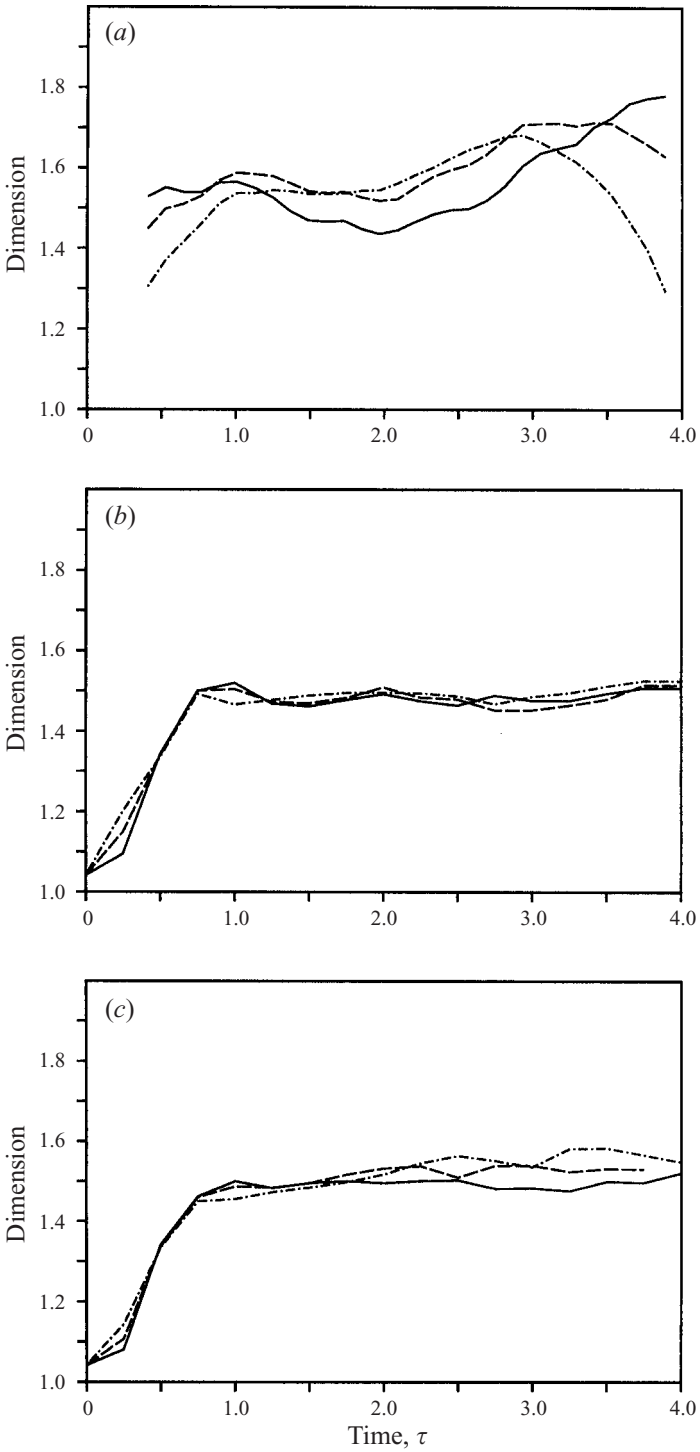

FIGURE 21. The dependence of the fractal dimension on the concentration C contour selected. (*a*) Experiments, (*b*) idealized simulations and (*c*) barrier simulations. Curves are shown for $C = 0.5$ (solid), $C = 0.375$ (dash) and $C = 0.25$ (dot-dash).

We thus find that all concentration contours are advected by turbulent motions with similar characteristics and produce a concentration-independent fractal dimension.

The structural differences between the two cases lead to further differences in the fractal nature of the flows. Catrakis & Dimotakis (1996) found the fractal dimension for plumes and jets to be scale dependent (i.e. $D(\varepsilon)$ is a non-constant function of ε), whereas the constant slope in figure 19 shows that the dimension is independent of scale for the present Rayleigh–Taylor instability. We suggest here that these differences are the result of the same correlation between concentration and turbulence found in plumes and jets but absent from Rayleigh–Taylor instability. In a plume or jet a typical iso-concentration contour will span a finite range of radii and, as a result, be subject to a range of statistically and structurally different turbulent eddies. Sections of the contour at smaller radii will experience more intense turbulence with a different structure (on average) than those sections at larger radii. The box counting algorithm will be biased at small scales towards the regions containing more highly contorted contours (i.e. smaller radii where the turbulence has a slower roll-off in the power spectrum) with the bias gradually changing as the scales increase. As a result the relationship between box count and box size is not the simple power law found in the more homogeneous Rayleigh–Taylor instability.

These arguments can be taken one step further to form the hypothesis that any correlation between the structure of the turbulence and concentration of some scalar will result in the fractal dimension for iso-concentration contours being (*a*) concentration dependent and (*b*) scale dependent. The converse, however, need not be true as a homogeneous flow need not produce a scale-independent fractal dimension.

The relationship between the velocity power spectrum and the fractal dimension of a marked line of fluid elements advected by a two-dimensional flow field is known (Vassilicos 1989) to be

$$P_u(k) \sim k^{D'-2}, \tag{9}$$

where D' is the co-dimension of the line and $P_u(k)$ is assumed to be constant in time between the point when the line is marked and the dimension measured.

This result has led to the (as yet unproven) suggestion (see Sreenivasan 1991) that, for the distortion of a surface by a three-dimensional flow, the fractal dimension and the slope of the power spectra may be related in the same way, with the dimension D_2 of the iso-concentration contours being related to the co-dimension D' of the surface by $D' = D_2 - 1$. For the present study the dimension is typically $D_2 \approx 1.47$ during the growth phase, a value which suggests velocity power spectra following $k^{-1.53}$. This result is consistent with the spectra inferred from the concentration measurements.

We need to be careful about how the arguments leading to (9) and its three-dimensional counterpart are applied to the evolving Rayleigh–Taylor instability. The fluid surface is marked at $\tau = 0$ and is advected by an evolving velocity field. During the early stages of this evolution the velocity power spectrum flattens towards a $k^{-5/3}$ relationship, resulting in a increase in the fractal dimension of some associated scalar. During this evolution the true fractal dimension could be seen only if new fluid lines or surfaces were marked at each stage. The surface marked by the density has been subjected to a range of different flow structures during its history and, as a result, any fractal dimension calculated from it will represent some weighted mean of what has gone before rather than being a snapshot of the current flow.

What allows us to use these data and, to a first approximation, ignore this evolution effect is the combination of an accelerating flow and diffusion of the measured concentration field. The acceleration of the flow means that the turbulence responsible

for the advection of the concentration field is more intense in the recent past than earlier in the evolution. As a result, the structure of the velocity field responsible for the recent advection is more important than the advection which occurred at earlier times. This biasing towards more recent advection is further assisted by diffusion of the measured scalar. This diffusion acts to erase information about advection at earlier times, especially at the finer scales.

The net effect of this evolution is likely to be minimal between $\tau = 1$ and $\tau = 2.5$ where we have seen that the statistical properties of the flow are approximately constant. At earlier and later times the effect of the evolution is likely to manifest itself as a lag in the measured fractal dimension. Note that similar arguments may be applied to the relationship between the concentration power spectra and the velocity field responsible for advecting it.

The dimension $D_2 \approx 1.47$ determined from these experiments is greater than the $D_2 \approx 1.3$ obtained by Linden *et al.* (1994). The significantly thicker light sheet and mismatched refractive indices used in the earlier study both lead to a blurring of the finer-scale features and hence the higher value of D_2 for the newer experiments. We believe $D_2 \approx 1.47$ reflects the structure of the instability more accurately.

7. Concentration statistics within the mixing zone

The ultimate effect of the growth of the mixing zone and the development of fine-scale three-dimensional structure is that significant mixing at a molecular level occurs. One way to quantify this is to construct the concentration probability density function. In addition, a molecular mixing fraction has been defined which gives an integrated estimate of the degree of molecular mixing.

7.1. *Probability density functions*

Linden *et al.* (1994) presented concentration probability density functions for their experiments and simulations, achieving a moderate level of agreement between them. With the improvements in the experimental techniques and the modelling of the experimental initial conditions, we are in the position to investigate this relationship further. As before a combination of ensemble and cross-tank averages are used to improve the statistical reliability of the data.

Figure 22 compares the concentration probability density functions for the three data sets in the same regions as used to calculate the power spectra. The curves have been normalized such that the integral of the area under each curve is unity. At $\tau = 1$ (figure 22*a*), all three show a slowly varying response over much of the concentration range, with the most noticeable feature being the sharp increase in probability density at high concentrations for the experiments and barrier simulations. This feature is due to the down-rush of upper-layer fluid adjacent to the right-hand endwall as the barrier is withdrawn. The same feature is not observed in the idealized simulations because the mixing occurs uniformly over the length of the tank. The experimental curve follows that for the idealized simulations more closely at $\tau = 2$ (figure 22*b*), at least for low concentrations. At higher concentrations, there is little to distinguish between the curves, except that the experiments and, to a lesser extent, the barrier simulations have a small bump near $C = 0.6$. The origin of this bump is unclear.

By $\tau = 3$ (figure 22*c*) the flow is influenced by the top and bottom of the tank. The curves for the simulations have broadened out, although the experimental curve is somewhat peaky. A similar peakiness was found by Linden *et al.* (1994; their

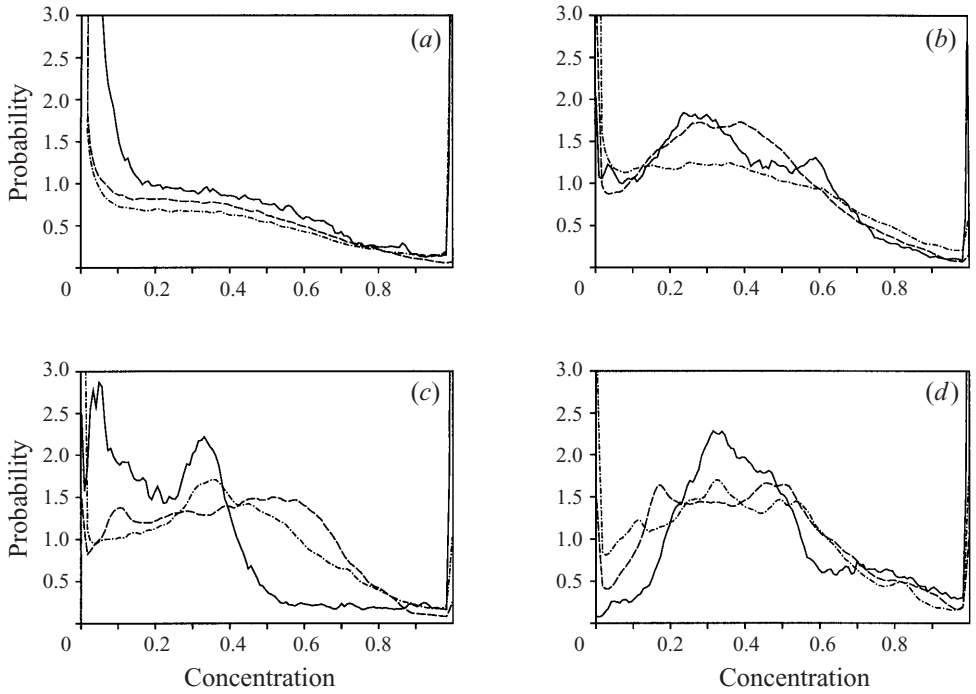

FIGURE 22. Comparison between the concentration probability density functions at (*a*) $\tau = 1$, (*b*) $\tau = 2$, (*c*) $\tau = 3$ and (*d*) $\tau = 4$ for the experiments (solid) and the simulations with idealized initial conditions (dashed) and using the barrier perturbation (dot-dash).

figure 10). While it could be argued that the barrier simulation follows the experiment the more closely of the two due to the presence of a peak around $C = 0.35$, the differences are too large to add much support for this. Similar arguments apply to $\tau = 4$ (figure 22*d*) with the experimental and barrier simulation peaks coinciding at around $C = 0.32$, but overall differences are larger than between the two simulations.

The clear differences between the simulations and experiments render it impossible to make a definitive statement that one type of simulation matches the experiments better than the other. These results suggest more that the use of probability density functions is not a good method for discriminating between the various scenarios. The experimental results are somewhat contaminated by the noise at the two ends of the tank, but this is thought to have only a small impact on the results presented here. The limited spatial resolution of the simulations may also play a role.

7.2. *Molecular mixing fraction*

The molecular mixing fraction,

$$\theta = \frac{\overline{\overline{C(1-C)}}}{\overline{\overline{C}}(1-\overline{\overline{C}})}, \tag{10}$$

is a measure of how well-mixed the two layers are on a given horizontal plane (Linden *et al.* 1994). The maximum value $\theta = 1$ will be achieved when the concentration is uniform across the plane. Here $\theta = \theta(z, \tau)$ and the double overbar represents averaging

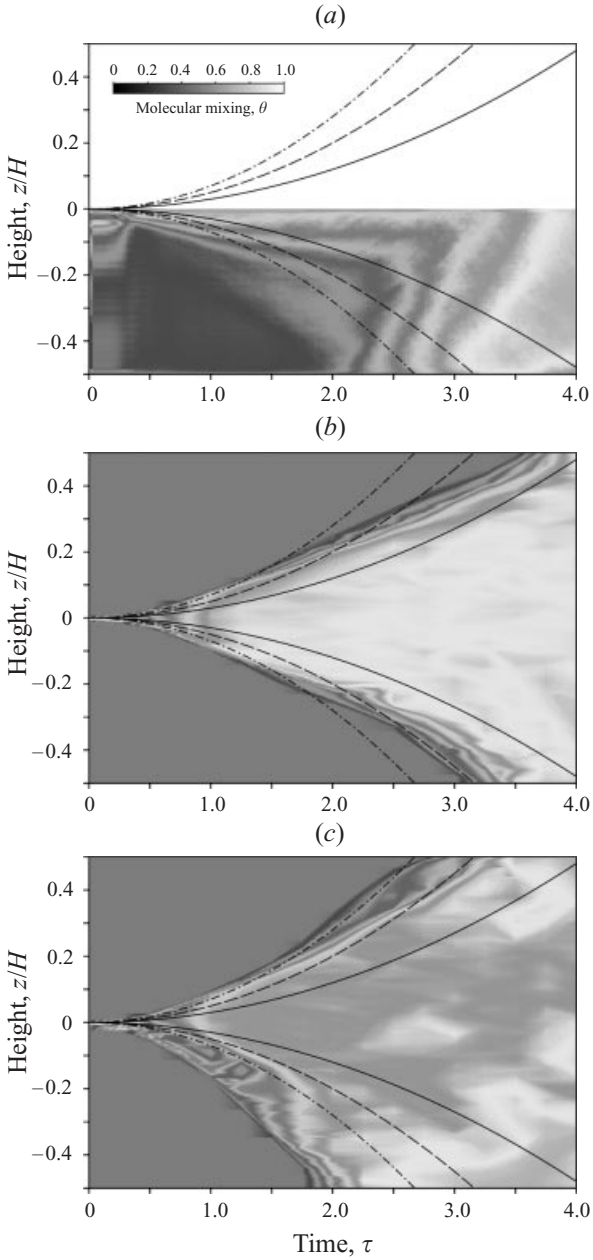

FIGURE 23. Evolution of profiles of the mean molecular mixing ratio $\hat{\theta}(z/H, \tau)$. (*a*) The experimental data, is averaged over the length of the tank and over the 16 experiment ensemble. The simulations are with (*b*) idealized initial conditions and (*c*) the measured initial conditions. For the simulations the data is averaged over the length and width of the flow domain. The superimposed curves represent the quadratic growth of the similarity law with values of $\alpha_i = 0.03$, 0.05 and 0.07 ($i = 1, 2$) for the solid, dashed and dot-dashed lines (respectively).

both along and across the flow domain (i.e. the average over a horizontal plane). To achieve consistency between the experimental and numerical data sets in the present paper, we calculate an equivalent molecular mixing fraction $\hat{\theta}(z, \tau)$ as the combined ensemble and/or cross-tank average of $\theta_x(z, \tau)$, where $\theta_x(z, \tau)$ is computed

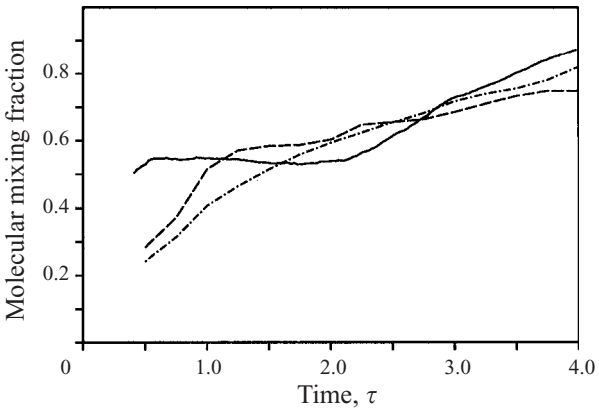

FIGURE 24. Time evolution of the global molecular mixing fraction $\hat{\Theta}(\tau)$. Experimental data is shown as solid lines, idealized simulations as dashes and barrier simulations as dot-dashed lines.

using along-tank averages only. In particular we use

$$\hat{\theta} = \left\langle \frac{\overline{C(1-C)}}{\overline{C}(1-\overline{C})} \right\rangle. \tag{11}$$

Figure 23 shows the molecular mixing profiles $\hat{\theta}(z,\tau)$ as greyscale images in a form analogous to the concentration profiles of figure 11. The experimental data in figure 23(*a*) show a similar pattern of growth of the mixing layer to the barrier simulations shown in figure 23(*c*). As expected the mixing layer can be seen to penetrate downward into the lower layer more rapidly than its upward growth. In contrast the idealized simulations of figure 23(*b*) shows a symmetric growth which is well-modelled by a quadratic time dependence as indicated by the superimposed curves. The experimental data and barrier simulations are less well-modelled by such a growth law and exhibit a more complex structure than the idealized simulations.

Linden *et al.* (1994) define the global molecular mixing fraction,

$$\Theta = \int_{-H/2}^{H/2} \overline{\overline{C(1-C)}}\,\mathrm{d}z \Big/ \int_{-H/2}^{H/2} \overline{\overline{C}}\,\overline{\overline{(1-C)}}\,\mathrm{d}z, \tag{12}$$

where $\Theta = \Theta(\tau)$, is a measure of the horizontal homogeneity and mixing for the entire domain. As with the molecular mixing profiles we must reconcile the differences between spatial and ensemble averaging and we compute an equivalent measure

$$\hat{\Theta} = \left\langle \int_{-H/2}^{H/2} \overline{C(1-C)}\,\mathrm{d}z \Big/ \int_{-H/2}^{H/2} \overline{C}\,\overline{(1-C)}\,\mathrm{d}z \right\rangle, \tag{13}$$

where $\hat{\Theta} = \hat{\Theta}(\tau)$ and the angular brackets in (13) represent ensemble and/or cross-tank averaging of the quotient of the integrals.

The global molecular mixing fraction increases with time as shown in figure 24. The idealized simulations produce a larger value of $\hat{\Theta}$ for $\tau \lesssim 2.5$, reflecting the greater horizontal homogeneity found in the absence of the barrier-induced initial perturbation. In the barrier simulations the mixing layer extends to the bottom of the tank earlier than for the idealized simulations, leading to the establishment of a more stable and horizontally homogeneous state earlier than in the idealized simulations, thus causing the relative increase in $\hat{\Theta}$ for the more complex initial conditions. We believe that in both

cases the numerical simulations underestimate $\hat{\Theta}$ at early time due to lack of resolution of the fine-scale structure. Towards the end of the similarity phase the calculated values of $\hat{\Theta}$ are similar to the asymptotic $\hat{\Theta} = 0.8$ reported by Linden *et al.* (1994) for well-resolved self-similar mixing. The experimental measurements of $\hat{\Theta}$ show a broad similarity with their numerical counterparts, but it is not possible to draw any firm conclusions due to the contamination of these results by noise in the intensity measurements.

8. Conclusions

Traditionally the analysis of Rayleigh–Taylor instability has concentrated on α_1 and α_2 growth rate constants when comparing flows with different setups and approaches. One of the aims of this paper has been to provide a much broader range of diagnostics for both the experiments and simulations, allowing additional insight into the physics and extending the breadth of any comparison. Through the use of image processing techniques we have been able to extract details of the structure of the concentration field within the mixing zone and provide, for the first time for a laboratory experiment, quantitative measurements of the power spectra and molecular mixing, and to obtain more reliable figures for quantities such as the penetration and fractal dimension.

Detailed numerical simulations were undertaken both to verify that the current generation of codes are able to provide quantitative agreement with experimental measurements (provided appropriate initial conditions are selected), and to allow a detailed comparison between the real, but non-ideal, experiments and the idealized instability starting from a purely random initial perturbation. Such idealized flows are difficult, if not impossible, to achieve in the laboratory environment and this two-pronged approach has enabled us to determine which features of the flow are sensitive to the initial conditions and which develop in a more universal, self-similar manner.

As we have seen in this paper, we have excellent quantitative agreement between most aspects of the experiments and simulations, yet we are unable to give a reasonable, unambiguous estimate for the α_2 growth rate. The difficulty stems from the inhomogeneous structure of the flow and the sensitivity of α_2 (and α_1) to the precise method by which it is calculated. Increased spatial resolution has lead to a decrease in the values of α_1 and α_2 obtained from simulations, and an extension of the range of times over which τ^2 behaviour is found, reflecting the reduction in numerical dissipation. Nevertheless, even with the highest-resolution simulations currently available, there is an ambiguity as to how the growth should be determined. While α_1 and α_2 may be a very simple measure of the development of the instability, we contend here that it is not such a useful measure. Detailed comparisons should include other measures of the structure of the evolving mixing zone and the internal structure and statistics of the flow in addition to the component of h_1 or h_2 exhibiting a quadratic time dependence.

A further example of why the quadratic growth constants α_1 and α_2 do not provide a good characterization of the flow is the similarity between the experiments, TURMOIL3D calculations and simpler two-dimensional calculations presented in § 4 (figure 7). Visual comparison of these two-dimensional simulations with their three-dimensional counterparts shows that the overall growth and large-scale structure are in close agreement, at least up to $\tau = 3$, and that measures of h_1 and h_2 (and hence α_1 and α_2) would be comparable while, at the same time, the finer scales and internal structure are completely lacking.

Integral measures of the penetration such as $h_{1,0}$ and $h_{1,1}$ may be more robust against statistical fluctuations, but if the flow does not emanate from spatially homogeneous initial conditions, they may provide an inappropriate vehicle for comparison of different flows. For simple comparisons between different sets of initial conditions, it is desirable to use more than one such measure as these different moments of concentration provide information about different aspects of the flow. We suggest that the scatter plots presented in figure 12 provide a broader base for comparison of both structure and growth rate.

Comparisons of the internal structure of the flow show that at small scales the memory of the initial conditions is rapidly lost and the flow exhibits the characteristics of scale-independent self-similarity and a fully developed turbulent spectrum. The agreement between the experiments and barrier simulations is excellent, given the limitations on the spatial resolutions in the simulations and signal noise in the experiments. Even the idealized simulations show a remarkable agreement in the internal structure (although the spatial resolution of these is more restrictive), suggesting the universal nature of the dynamics within this region. The main differences arise after the mixing region extends to the bottom of the tank (and the un-modelled three-dimensional component of the initial conditions becomes important), and from absolute quantities such as the probability density functions which show a sensitivity to fine details of the initial conditions but not to the gross features of the flow.

The level of statistical agreement between experiments and three-dimensional simulations reflects the resolution at which the simulations were undertaken. If the resolution were to be increased for a three-dimensional simulation, we would expect very little difference in the growth of the mixing zone but there would be some differences in the internal structure. In particular we would expect the self-similarity found in both the simulations and experiments to extend to higher wavenumbers and smaller length scales, with little differences at the lower wavenumbers and larger length scales. Growth rates, spectral slopes, fractal dimensions and molecular mixing fractions are all expected to remain much the same.

Correct modelling of the initial conditions is critical if the gross features of the numerical simulations are to agree, even qualitatively, with experimental, industrial or natural manifestations of Rayleigh–Taylor instability. This modelling need not include all the scales found in the real initial conditions. The turbulent nature of the flow causes the memory of the finer details of the initial conditions to be lost very quickly. This loss of memory allows artificial noise to be used to model the fine-scale component of the initial conditions. Although matching the amplitude of this noise would be desirable, at least at the larger length scales, the present work has shown that it is not essential. Once the flow becomes nonlinear, the turbulent interactions rapidly fill any gaps in the spectra and provide a continuous wavenumber dependence.

In most studies of Rayleigh–Taylor instability the initial conditions have been characterized purely in terms of their power spectra with an implicit assumption that the phase relationship between the modes is unimportant. If this assumption is true, then the spatial structure of the initial perturbation will not affect the averaged properties or the internal details of the subsequent flow. However, the local nature of baroclinic generation of vorticity compared with the more global nature of the Fourier power spectra lead us to question the validity of this assumption.

The phase relationship becomes particularly important when considering flows with a well-defined initial structure such as that produced in these experiments by an interaction between the flow induced by the barrier and the endwalls of the tank.

Simulations have shown that a range of different flows and growth rates may be produced by changing the phases of the various Fourier modes used to describe the initial conditions. If the initial conditions are more homogeneous, external measures of the flow may differ significantly from those produced by the barrier simulation (e.g. the rate of growth of the extremes of the mixing zone), although some of the mean statistics may be comparable. As we have seen, the internal structure of the concentration field does not retain a memory of the initial conditions, yielding a close similarity in these aspects regardless of the phase of the initial conditions.

The external features of the flow are controlled primarily by the larger scales in the initial conditions as these are more energetic and robust to nonlinear interactions and thus the corresponding features survive as identifiable structures for much longer than the finer-scale components of the instability. Indeed the ensemble of experiments has shown that while precise details of the initial conditions vary from one realization of the flow to the next, the larger scales and the overall development of the instability are similar across the ensemble. It is thus unnecessary to model the initial conditions with a high degree of accuracy. Moreover, we have shown that replacing the finer-scale components of the initial perturbation with random noise while retaining the larger-scale two-dimensional component provides a set of initial conditions which evolve numerically in much the same way as the corresponding experiments.

The initial conditions perturb the flow away from a horizontal interface between the two layers, thus allowing the baroclinic generation of vorticity. The spatial structure of the perturbation sets the spatial structure of the vorticity which subsequently drives the flow. In contrast, the amplitude of the perturbation is much less important. The amplitude sets the initial rate at which the baroclinic torque will generate vorticity, but it does not directly affect the spatial distribution of this vorticity and the initial linear phase of vorticity generation will take place regardless of the (non-zero) amplitude of the perturbation. This baroclinically generated vorticity soon starts to drive the flow, the vorticity having grown to levels much higher than that contained in the initial perturbation. The subsequent growth of the instability is only weakly dependent on the amplitude of the initial perturbation.

Determining the initial conditions as an ensemble mean of experimental initial conditions would be a reasonable option if there were random component with an intermediate to large-scale structure and amplitude comparable with the variation between experiments in the ensemble. For the present work, the ensemble mean of the initial conditions measured in the homogeneous case reproduces the largest-scale overturning mode, but the amplitude of the smaller-scale components (particularly the pronounced $k/k_0 \approx 5$) is considerably reduced due to small phase differences between different realizations within the ensemble. It is thus more meaningful to perform an ensemble of simulations, each with a slightly different structure to their initial conditions, than to do a single simulation starting from the ensemble mean.

We have modelled explicity only the two-dimensional component of the experimental initial conditions. This approach has clearly been successful (at the centreplane) until after the mixing zone has extended through the entire depth of the tank. It is not so successful near the front and back walls, or at later times due to the significant but neglected three-dimensional component introduced by the unprotected strips down either side of the barrier. We suggest that if a similar level of modelling of this component were to be included we would see a corresponding improvement in the agreement near the walls and at late times.

Detailed comparisons of the type presented here are still relatively rare. We expect

they will become of increasing importance to both the experimental and the computational fluid dynamics communities as the technologies available for both aspects of the work improve. An important component of such studies will be detailed analysis of the initial and boundary conditions. In many cases a relatively crude level of modelling will be all that is required. Matching the conditions in unstable flows is more likely to be important due to the amplifying effect inherent in most instabilities. As we have seen, such matching can lead to a dramatic improvement in the quantitative agreement between the two approaches.

S. B. D. wishes to acknowledge the financial support of AWE Aldermaston and the Isaac Newton Trust.

REFERENCES

Andrews, M. J. & Spalding, D. B. 1990 A simple experiment to investigate two-dimensional mixing by Rayleigh–Taylor instability. *Phys. Fluids* A **6**, 922–927.

Andronov, V. A., Bakhrakh, S. M., Meshkov, E. E., Mokhov, V. N., Nikiforov, V. V., Pevnitskii, A. V. & Tolshmyakov, A. I. 1976 Turbulent mixing at contact surface accelerated by shock waves. *Sov. Phys. JETP* **44**, 424–427.

Catrakis, H. J. & Dimotakis, P. E. 1996 Mixing in turbulent jets: scalar and isoscalar measures. *J. Fluid Mech.* **317**, 369–406.

Chandrasekhar, S. 1961 *Hydrodynamic and Hydromagnetic Stability*. Oxford University Press.

Dalziel, S. B. 1992 Decay of rotating turbulence: some particle tracking experiments. *Appl. Sci. Res.* **49**, 217–244.

Dalziel, S. B. 1993 Rayleigh–Taylor instability: experiments with image analysis. *Dyn. Atmos. Oceans* **20**, 127–153.

Dalziel, S. B. 1994*a* Perturbations and coherent flow in Rayleigh–Taylor instability. In *4th Intl Workshop on the Physics of Compressible Turbulent Mixing, Cambridge University* (ed. P. F. Linden, D. L. Youngs & S. B. Dalziel), pp. 32–41.

Dalziel, S. B. 1994*b* Final report: Molecular mixing in Rayleigh–Taylor instability. Report for AWE, 91 pp.

Dimonte & Schneider, G. 1996 Turbulent Rayleigh–Taylor instability experiments with variable acceleration. *Phys. Rev.* E **54**, 3740–3743.

Kucherenko, Yu, Shibarshov, L. I., Chitaikin, V. I., Balabin, S. I. & Pylaev, A. P. 1991 Experimental study of the gravitational turbulent mixing self-similar mode. In *3rd Intl Workshop on the Physics of Compressible Turbulent Mixing, Cambridge University* (ed. R. Dautray), pp. 427–454.

Lane-Serff, G. F. 1989 Heat flow and air movement in buildings. PhD thesis, DAMTP, University of Cambridge.

Lane-Serff, G. F. 1993 Investigation of the fractal structure of jets and plumes. *J. Fluid Mech.* **249**, 521–534.

Leer, B. van 1977 Towards the ultimate conservative difference scheme IV. A new approach to numerical convection. *J. Comput. Phys.* **23**, 276–299.

Linden, P. F., Redondo, J. M. & Youngs, D. L. 1994 Molecular mixing in Rayleigh–Taylor instability. *J. Fluid Mech.* **265**, 97–124.

Rayleigh, Lord 1883 Investigation of the character of the equilibrium of an incompressible heavy fluid of variable density. *Proc. Lond. Math. Soc.* **XIV**, 70–177. *Reprinted in Scientific papers* Vol. II, pp. 200–207. Cambridge University Press, 1900.

Read, K. I. 1984 Experimental investigation of turbulent mixing by Rayleigh–Taylor instability. *Physica* D **12**, 45–58.

Redondo, J. M. & Linden, P. F. 1990 Geometrical observations of turbulent density interfaces. In *Proc. IMA Conf. on Mathematics and Computations of Deforming Surfaces* (ed. J. C. R. Hunt, D. G. Dritschel & R. J. Perkins). Oxford University Press.

Sharp, D. H. 1984 An overview of Rayleigh–Taylor instability. *Physica* D **12**, 3–18.

Simpson, J. E. & Linden, P. F. 1989 Frontogenesis in a fluid with horizontal density gradients. *J. Fluid Mech.* **202**, 1–16.

Sreenivasan, K. R. 1991 Fractals and multifractals in fluid turbulence. *Ann. Rev. Fluid Mech.* **23**, 539–600.

Taylor, G. I. 1950 The instability of liquid surfaces when accelerated in a direction perpendicular to their planes. *Proc. R. Soc. Lond.* A **201**, 192–196.

Tennekes, H. & Lumley, J. L. 1972 *A First Course in Turbulence*. MIT Press.

Vassilicos, J. C. 1989 On the geometry of lines in two-dimensional turbulence. In *Advances in Turbulence 2*, (ed. H.-H. Fernholtz & H. E. Fiedler), pp. 404–411. Springer.

Voropayev, S. I., Afanasyev, Y. D. & Heijst, G. J. F. van 1993 Experiments on the evolution of gravitational instability of an overturned initially stably stratified fluid. *Phys. Fluids* A **5**, 2461–2466.

Youngs, D. L. 1989 Modelling turbulent mixing by Rayleigh–Taylor instability. *Physica* D **37**, 270–287.

Youngs, D. L. 1991 Three-dimensional numerical simulation of turbulent mixing by Rayleigh–Taylor instability. *Phys. Fluids* A **3**, 1312–1320.

Youngs, D. L. 1994*a* Numerical simulation of mixing by Rayleigh–Taylor and Richtmyer–Meshkov instabilities. *Lasers and Particle Beams* **12**, 725–750.

Youngs, D. L. 1994*b* Direct three-dimensional numerical simulation of mixing by Rayleigh–Taylor instability. In *4th Intl Workshop on the Physics of Compressible Turbulent Mixing, Cambridge University* (ed. P. F. Linden, D. L. Youngs & S. B. Dalziel), pp. 167–177.